University of Strathclyde
Department of Physics

A High-Energy Resolution X-Ray Spectrometer with Interchangeable Detectors (HEX-ID) for Short-Pulse Laser-Plasma Experiments

by
David Fraser Martin

A thesis presented in fulfilment of the requirements for the degree of Master of Philosophy

2012

This thesis is the result of the author's original research. It has been composed by the author and has not been previously submitted for examination which has led to the award of a degree.

Signed:  Date: 6th April 2012

ACKOWLEDGEMENTS

Thanks must first go to Anthony Meadowcroft (AWE) for his preparation and organisation of the project, and outlining the key topic areas that were to be covered in order to successfully design the HEX-ID spectrometer, a pioneering target diagnostic for short-pulse laser-plasma experiments. A brief summary of his project plan has been included in *Appendix A.1* for reference. He provided key physics related background information and contributed many ideas to the design from his previous diagnostic design experience.

Thank you to Prof. Paul McKenna and Dr. David Carroll (University of Strathclyde) for supervising me from afar this past year, and assisting me to be accepted to the ICOPS 2011 conference where the design of the HEX-ID was first presented to the international plasma physics community. Thanks to Dr. Gordon Robb who provided important information on the postgraduate requirements of University of Strathclyde.

There are several members of Ray Edward's team at AWE who contributed to this research. The experimental work undertaken in this project could not have been done without the help and guidance of Lisa Peacock and Chris Bentley. Lisa spent numerous hours working with me in the Mason x-ray laboratory exposing, scanning and processing image plates. Chris initially supervised me operating the Excalibur x-ray facility for the crystal reflectivity experiments, and then trained me to use it in his absence. Dave Drew was a very valuable member of the team writing the software to operate the detector hardware (CompactRIO controller and CMOS sensors), and assisting in installing and testing the wiring required for this. James Palmer and Ray Long provided interesting discussions on laser systems and electronic components respectively. Ray continues to be involved in the building of a test box for the electronics.

Finally, I am grateful to the Plasma Physics Department at AWE for funding this project and to Department of Physics at University of Strathclyde for hosting this MPhil degree.

ABSTRACT

High resolution, soft x-ray spectroscopy is a useful and flexible diagnostic technique which has been applied to plasma physics experiments for many years. Examples of previous instruments that have utilised the technique include the Henway [1] spectrometer developed at LLNL, and later the HENEX [2] spectrometer, which has been fielded on experiments at both OMEGA and NIF.

The design of these previous x-ray spectrometers has been analysed in order to produce a four channel high-energy x-ray spectrometer (HEX-ID) with superior resolution. The shielding has been adapted for use on short-pulse laser-plasma experiments. HEX-ID is intended for: analysis of characteristic x-ray line spectra from backlighter materials (laser irradiated materials producing x-rays to interact with a secondary target); identification of plasma ion species and their charged states; measurement of plasma opacity and of the absolute conversion efficiency of characteristic x-ray line emissions. The spectrometer will be fielded at the new Orion laser facility at AWE (UK) and at OMEGA (USA).

The minimum theoretical resolving power, $E/\delta E$, of HEX-ID (~730) has been improved upon that of HENEX (~500). The enhancement in resolving power has been achieved by reducing the crystal radius-of-curvature and allowing a variation in the crystal-to-detector distance, which can be manually set before TIM-based deployment. Four convex reflection crystals provide a total spectral range of approximately 1.2 to 9.8 keV in overlapping bands. The crystals were characterised using the Excalibur soft x-ray facility at AWE to determine their reflectivity values for a range of x-ray energies. In order to achieve a desired spectral and temporal resolution, adapt the spectrometer dynamic range to long-pulse and short-pulse laser shots, as well as for cross-channel comparison of the energy dispersion and spectral range, HEX-ID can utilize a number of detectors. These are image plate, CMOS and PCD. The spatial resolution of different IP systems was investigated, which indicated the FUJI BAS TR IP scanned with the Fuji FLA7000 scanner is best. Spatial resolution tests were also carried out with the CMOS sensors to compare to the IP.

CONTENTS

FIGURES & TABLES

ABBREVIATIONS

AWE	Atomic Weapons Establishment
BAS	Biological Analysis System
CAD	Computer Aided Design
CCD	Charge Coupled Device
CMOS	Complementary Metal Oxide Silicon
CPA	Chirped Pulse Amplification
cRIO	CompactRIO
CsI:Tl	Columnar-grown Cesium Iodide doped with Thallium
CTBT	Comprehensive Test Ban Treaty
CTF	Contrast Transfer Function
CW	Continuous Wave
dc	Direct Current
DEF	Direct Exposure Film
EDS	Energy Dispersive X-ray Analysis
EMI	Electromagnetic Interference
EMP	Electromagnetic Pulse
FPGA	Field-Programmable Gate Array
Gd_2O_2S:Eu	Gadolinium Oxysulphide doped with Europium
Gd_2O_2S:Tb	Gadolinium Oxysulphide doped with Terbium
HDPE	High Density Polyethylene
HEDP	High Energy Density Physics
HENEX	High Energy Electronic X-ray Spectrometer
HEX-ID	High Energy X-ray with Interchangeable Detectors Spectrometer
ICF	Inertial Confinement Fusion
IP	Image Plate
KDP	Potassium Dihydrogen Phosphate
LLNL	Lawrence Livermore National Laboratory
MCA	Multichannel Analyser
Nd:glass	Neodymium-doped Glass
Nd:YAG	Neodymium-doped Yttrium Aluminium Garnet

Nd:YLF	Neodymium-doped Yttrium Lithium Fluoride
NI	National Instruments
NIF	National Ignition Facility
NIST	National Institute of Standards and Technology
NRL	Naval Research Laboratory
OPCPA	Optical Parametric Chirped Pulse Amplifer
PAM	Pre-Amplifier Module
P-C	Proportional Counter
PCD	Photo-Conducting Diamond
PMT	Photo-Multiplier Tube
PPD	Plasma Physics Department
PSL	Photo-Stimulated Luminescence
RAL	Rutherford Appleton Laboratory
RSG	Radiation Science Group
TCC	Target Chamber Centre
TDAS	Target Data Acquisition System
Ti:sapphire	Titanium Sapphire
TIM	Ten Inch Manipulator

1.0 INTRODUCTION

1.1 Laser-Produced Plasma

Focussing very intense laser light onto solid targets or gas plumes causes rapid heating and ionization of the medium to create plasma. The plasma is heated to very high temperatures as it absorbs increasing amounts of laser energy. The hot plasma expands away from the surface into the vacuum of the target chamber. In large laser facilities, the laser(s) can deposit a great deal of energy onto the target in a very short period of time, typically hundreds of joules of energy in a time of the order of nanoseconds (long-pulse lasers). Focussing these pulses down to an area of tens of microns across results in very high irradiances of the order 10^{15} Wcm^{-2} or greater. [3]

The size of the plasma produced is determined by the laser spot size [4]. The duration of laser pulses can vary considerably between experiments with long pulses (ns) being used for Inertial Confinement Fusion (ICF) experiments and short pulses (ps) are used for other experiments [5]. Applications of high power lasers include ICF, laboratory astrophysics, compact particle accelerators and radiation sources, and many fundamental studies of hot, dense matter [6]. *Figure 1* shows a schematic diagram of a short-pulse laser striking a solid target and examples of the products given off from that interaction.

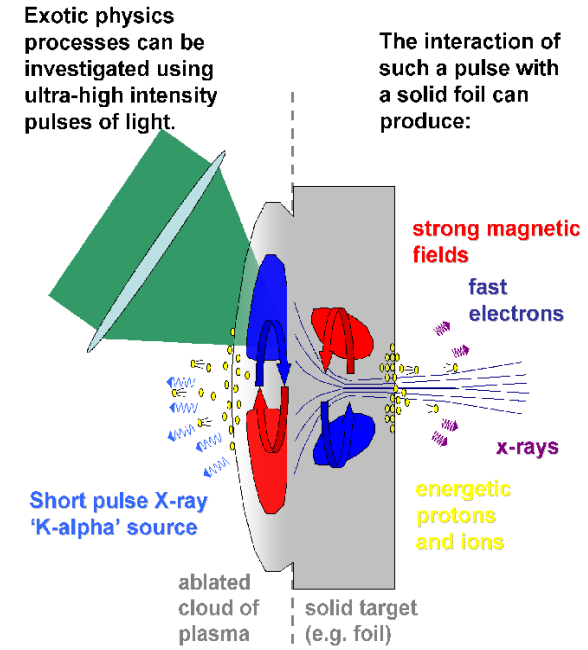

Figure 1: Schematic of a short-pulse laser matter interaction and the products. [7]

Fast electrons are produced when electrons removed from atoms due to the strong electric field strength at the laser focus, are accelerated. Very large magnetic fields are created due to the electric current produced by the large number of electrons travelling in the material. Kα x-rays are the energy released when electrons transition from the second shell of an atom to the inner shell in order to replace one that has been removed. These x-rays have a characteristic energy for different elements. Protons and ions accelerate from the rear surface of the target towards the electrons as they are ejected the target. A wide range of energies on the electromagnetic spectrum are emitted from a laser-produced plasma. *Figure 2* shows a typical radiation spectrum compared to that of a blackbody at the same temperature showing the range covered.

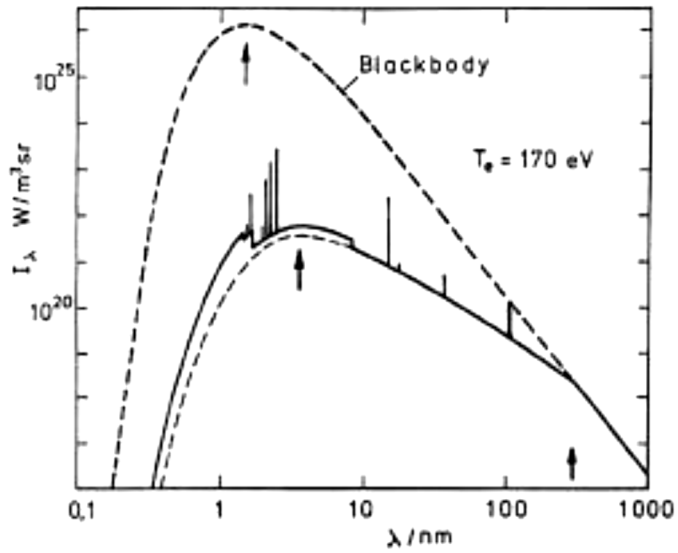

Figure 2: Schematic radiation spectrum from a laser-produced plasma compared to that of a blackbody at the same temperature. [4]

1.2 High Power Laser Facilities

Plasma physics research is a crucial part of enabling AWE to design and underwrite a nuclear deterrent in the absence of underground testing. Previously, before the ratification of the Comprehensive Test Ban Treaty (CTBT) came into force, experiments in this field were carried out as part of the underground nuclear test programme. High energy density physics (HEDP) phenomena can be investigated with the use of high power laser facilities that can generate conditions within a laboratory which are similar to those in an exploding nuclear weapon. The HEX-ID diagnostic will be fielded on two high-power laser facilities – Orion in the UK and OMEGA in the USA. Both these facilities use similar Ten-Inch Manipulator (TIM) deployment systems, which allow diagnostics to be inserted without breaking the target chamber vacuum.

1.2.1 Orion

The Orion laser facility (*Figure 3*) is currently under commissioning at AWE, Aldermaston. Orion consists of ten long-pulse (ns) beams, and two short-pulse (ps) beams. The long-pulse beams, which are optimised for 1 ns square pulses, each deliver 500 J at 351 nm while the short-pulse beams both deliver 500 J around 1054 nm with a pulse length adjustable between 0.5 ps and 20 ps.

Each of the long-pulse beams has four stages to it: pulse generation; the pre-amplifier module (PAM); the disk amplifiers; and then beam transport to target. The initial source of the long-pulse beams is a commercial, distributed feedback fibre laser which delivers up to 1 W of continuous wave (CW) power at 1053 nm. The PAMs house a flash lamp pumped Nd:YLF rod and supporting systems. The output from the PAMs is relayed into four disk amplifiers, each housing three Nd:glass slabs (LG770). The output is about 750 J with a beam diameter of 300 mm. Frequency tripling is carried out using a pair of KDP crystals before the beam is transported to the target chamber. [8]

The two short-pulse beamlines are seeded by a common commercial Ti:sapphire system. The optical parametric chirped pulse amplifier (OPCPA) systems for both beamlines are pumped by a single, commercially-sourced Nd:YAG system that operates at the second harmonic. A four-passed, mixed glass rod amplifier subsystem uses phosphate and silicate glass. The disk amplifier chain then follows to increase the aperture to 200 mm. The beams are ultimately expanded to 600 mm before passing into each compressor vessel and then transported to the target chamber. [8]

Isochoric heating of targets will occur as the long pulse beams are used to compress the target, and then the short pulse beams are used to heat it very rapidly. A wide range of temperatures and pressures can be explored with Orion. Up to 15% of the Orion beam-time will be available to academic researchers from universities for collaborative experiments. [9, 10]

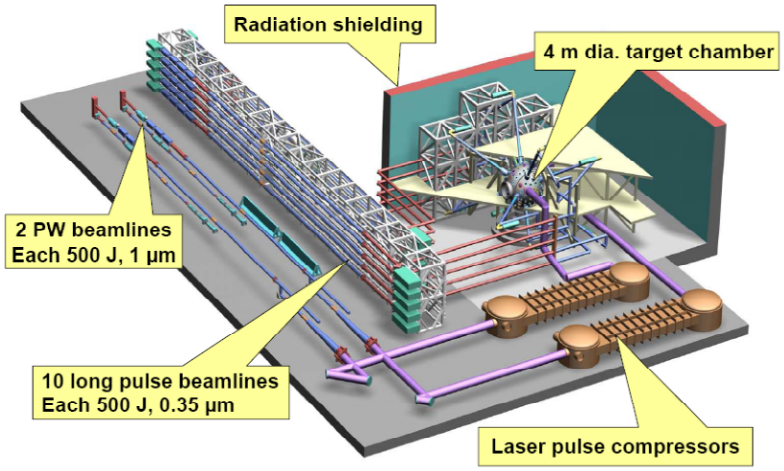

Figure 3: Schematic drawing of inside the Orion laser facility showing the laser hall, compressor hall and target hall. [11]

1.2.2 OMEGA

The OMEGA laser facility (*Figure 4*) at the University of Rochester Laboratory for Laser Energetics (LLE) has 60 long pulse laser beams which can provide up to 40 kJ of energy onto the target. OMEGA EP is an additional facility attached to OMEGA which provides short pulse capabilities to complement the long pulse beams. These beams can be used on a separate target chamber or diverted to the main target chamber for investigation of high-temperature and high-density regimes. [12]

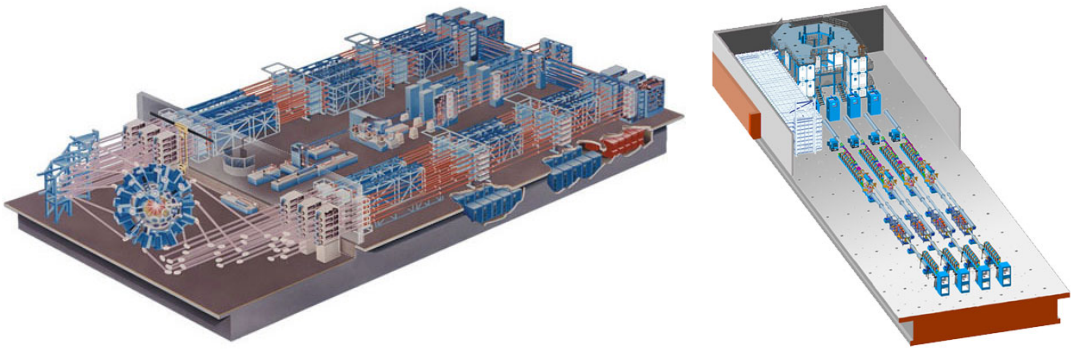

Figure 4: Schematic drawing of the OMEGA laser facility (left) and the OMEGA EP laser facility (right) at Laboratory for Laser Energetics. [12]

1.3 Diagnosing Laser-Produced Plasma

As seen in *Figure 1*, fast electrons, x-rays, and energetic protons and ions are given off during the interaction of a short-pulse laser with a solid foil target. A large range of diagnostic instrumentation is required given the variety of products emitted from the laser-target interaction. The plasma may then be appropriately diagnosed.

1.3.1 Diagnostic Instruments

The diagnostics being developed at AWE for Orion fall into three categories – optical, particle and x-ray diagnostics. Optical diagnostics include: optical streak cameras; passive shock breakout; optical pyrometry; active shock breakout; VISAR interferometer; and backscatter (SRS + SBS). Particle diagnostics include: electron spectrometers; neutron time-of-flight; total neutron yield; and neutron spectrometer. X-ray diagnostics include: x-ray microscopes; Dante; filter fluorescer; framing cameras; streak cameras; transmission grating spectrometer; Harada grating spectrometer; and hard x-ray spectrometer. [11]

1.3.2 X-ray Spectroscopy

X-ray spectroscopy is an invaluable diagnostic technique in the study of laser-produced plasma. Spectroscopic instruments can be used to measure the relative heights and widths of spectral features to provide information about the plasma conditions. This includes: analysis of characteristic x-ray line spectra from backlighter materials (materials irradiated with lasers beams in order to produce x-rays, which then interact with the target rather than the laser beams directly [13]); identifying plasma ion species and their charged states; measuring plasma opacity; and measuring the absolute conversion efficiency of characteristic x-ray line emissions.

1.3.3 Henway & HENEX X-ray Spectrometers

The Henway spectrometer [1] (*Figure 5*) was used at Lawrence Livermore National Laboratory (LLNL) on the NOVA laser and then with OMEGA at the Laboratory for Laser Energetics. More recently, the HENEX spectrometer [2] (*Figure 5*) was specially made as a diagnostic for the National Ignition Facility (NIF), but was also designed to fit into a TIM module for use on the OMEGA laser. Both these diagnostics use four channels with a convex reflection crystal in each to disperse soft x-ray energies of approximately 1 to 10 keV onto detectors. There was some overlap between the four energy bands to aid relative crystal calibrations. Each crystal in HENEX has a radius of curvature of 127 mm, while the radii of each crystal varied in Henway.

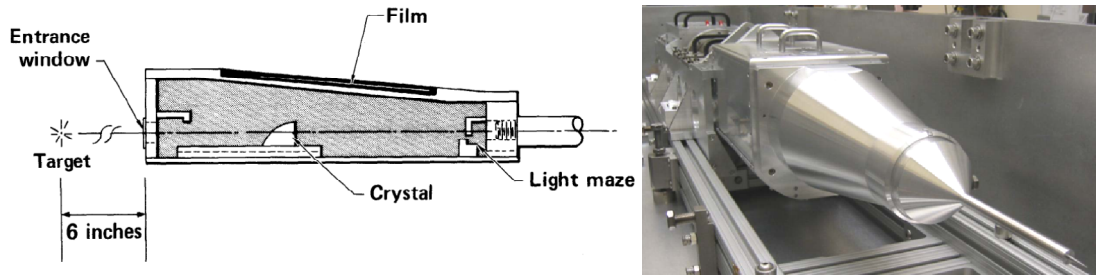

Figure 5: Schematic of the Henway spectrometer [14] (left) and photo of the completed HENEX spectrometer [15] (right).

Henway made use of direct exposure film (DEF) with a grain size of 1.6 μm, which was digitized using a microdensitometer after exposure. A light-tight filter located over the entrance aperture prevented the direct illumination of the film by x-rays. HENEX used complementary metal-oxide silicon (CMOS) electronic detectors, with a pixel size of 48 μm, coated with a scintillator material. The thickness of Gadolinium Oxysulphide doped with Europium (Gd_2O_2S:Eu) deposited on the detector faces was optimized for the spectral range to convert the x-rays to visible light.

HENEX required shielding to ensure the spectrometer components such as crystals and electronics were not damaged during the laser shots. ICF, for example, will produce high-energy electrons, x-rays, neutrons, electromagnetic interference (EMI) and debris. A lead faceplate, containing apertures for each channel, collimated the x-rays, reducing scattering contributions and a nosecone section was filled with high density polyethylene to absorb neutrons. The entire instrument was enclosed in an electrically conductive skin, serving as a Faraday cage, to shield the instrument for electromagnetic interference and pulses. An internal power supply (batteries) and fibre optic communications ensured no electrically conductive connection to the instrument in the TIM from the control station.

1.4 User Requirements for HEX-ID

Before the construction of Orion, laser-plasma experiments were carried out on the HELEN laser system at AWE. A CPA (chirped pulsed amplification system) short-pulse laser system upgrade was added to HELEN during the final years of its operation. It was during these experiments that the need for high resolution, soft x-ray spectroscopy in the range of 1 to 10 keV was identified, a range that had not been included in the original suite of Orion target diagnostics. Analysis of Henway and HENEX was undertaken to design a new spectrometer called HEX-ID (High-Energy Resolution X-ray with Interchangeable Detectors spectrometer).

The user requirements for the HEX-ID diagnostic set out at the start of the design process are as follows [16]:

1. The HEX-ID diagnostic will be TIM-compatible. It will be fielded for short-pulse and long-pulse laser shots at Orion by the Plasma Physics Group and at OMEGA by the Radiation Science Group so must meet the requirements of the TIMs at both facilities.
2. The HEX-ID diagnostic will be designed for very high resolution ($E/\delta E > 300$) x-ray spectroscopy of both short-pulse and long-pulse laser-target interactions. An improvement of the resolution capabilities is desired compared to previous, similar diagnostics of Henway and HENEX.

3. The HEX-ID diagnostic will be a pointable instrument. Fielding distance from the target will be determined by the deployment/retraction of the TIM payload boat and/or the target chamber size. It must be able to be aligned accurately and easily to the target before a laser shot is fired.
4. The detectors will be interchangeable to improve resolving power, adapt the dynamic range to a given laser shot, characterise the channels energy dispersion and spectral range, in addition to attaining the desired spectral and temporal resolution. The detectors used may include film, image plate, CCD sensors, CMOS sensors or others that are suitable.
5. An x-ray spectral range of 1 to 10 keV is required. A set of four convex reflection crystals will be used to provide the required spectral range. There is no requirement to examine x-rays outside this range as they will be covered by other diagnostics.
6. The HEX-ID diagnostic will need to be vacuum compatible as it will be deployed inside the target chamber after it has been evacuated of air allowing soft x-rays to propagate to the diagnostic.
7. A resolution $E/\delta E$ of > 1000 is desired. The resolution should be a maximum over smaller energy ranges to observe time-integrated x-ray line emissions such as the Kα and the Lα components.
8. The channels shall use convex reflection crystals which may be compactly mounted into the TIM payload boat. The reasoning behind the choice of four convex reflection crystals will be explained in *Chapter 2*.
9. The HEX-ID diagnostic shall have sufficient shielding to mitigate background signals present in the short-pulse and long-pulse laser-plasma environments. Due to the close proximity of the diagnostic to the target and the vulnerable components within, all potential sources of damage must be investigated and measures put in place to minimise or eradicate the risks.

The HEX-ID diagnostic will be utilised on many experiments and must be capable of being used to:

1. Observe x-ray emission lines to determine the thermodynamic state of the emitting plasma.
2. Measure the opacity of the plasma (how resistant it is to transmit radiation of a particular wavelength).
3. Verify x-ray backlighter materials (laser irradiated materials producing x-rays to interact with a secondary target).
4. Perform absolute conversion efficiency measurements of laser energy to x-rays from a solid target.
5. Identify plasma ion species and their charged states by using the relative heights and widths of spectral features.

2.0 DESIGN

This chapter provides key information on the design of HEX-ID and how it meets the user requirements that were set out at the start of the project. The areas of the design are outlined in the functionality diagram of the diagnostic (*Figure 6*).

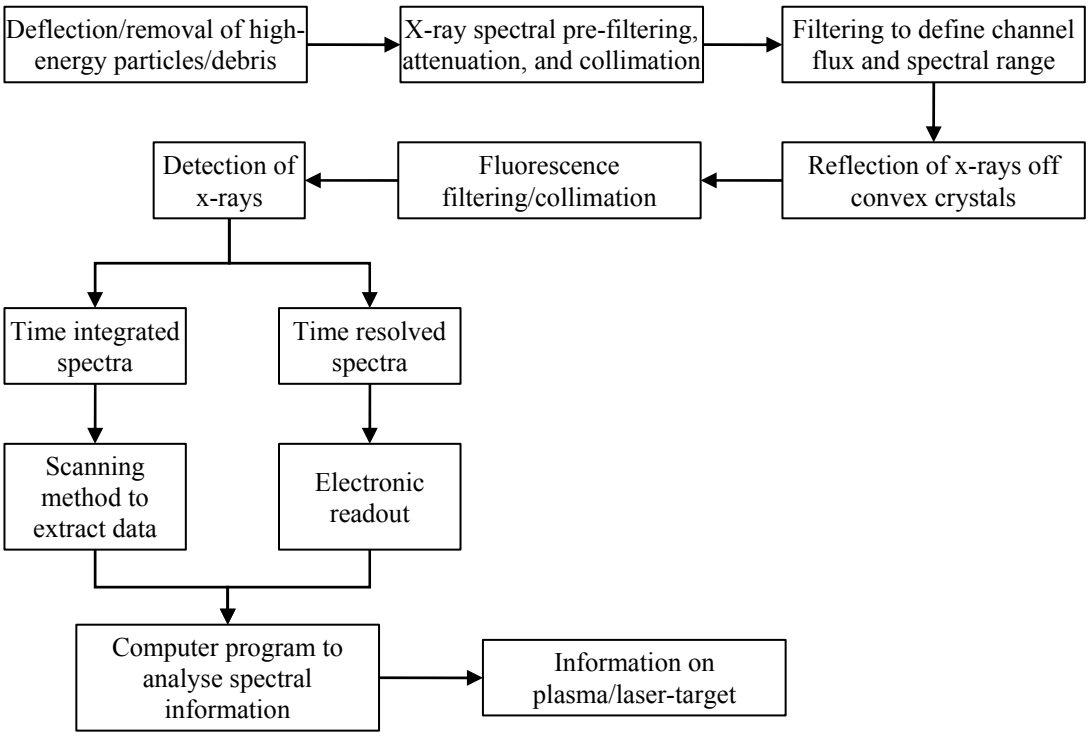

Figure 6: Functional breakdown diagram of the HEX-ID diagnostic.

In this section each stage of the functional breakdown above will be considered in turn from extraction, collimation and filtering of soft x-rays to reflection by convex reflection crystals onto a number of possible detectors giving time-integrated and time-resolved information for computer analysis. The electromagnetic shielding implemented, the anticipated signal level from each of the detectors, and further design considerations of HEX-ID will also be detailed. *Figure 7* shows the latest CAD drawings of HEX-ID within the TIM payload boat and the front portion only, providing more detail.

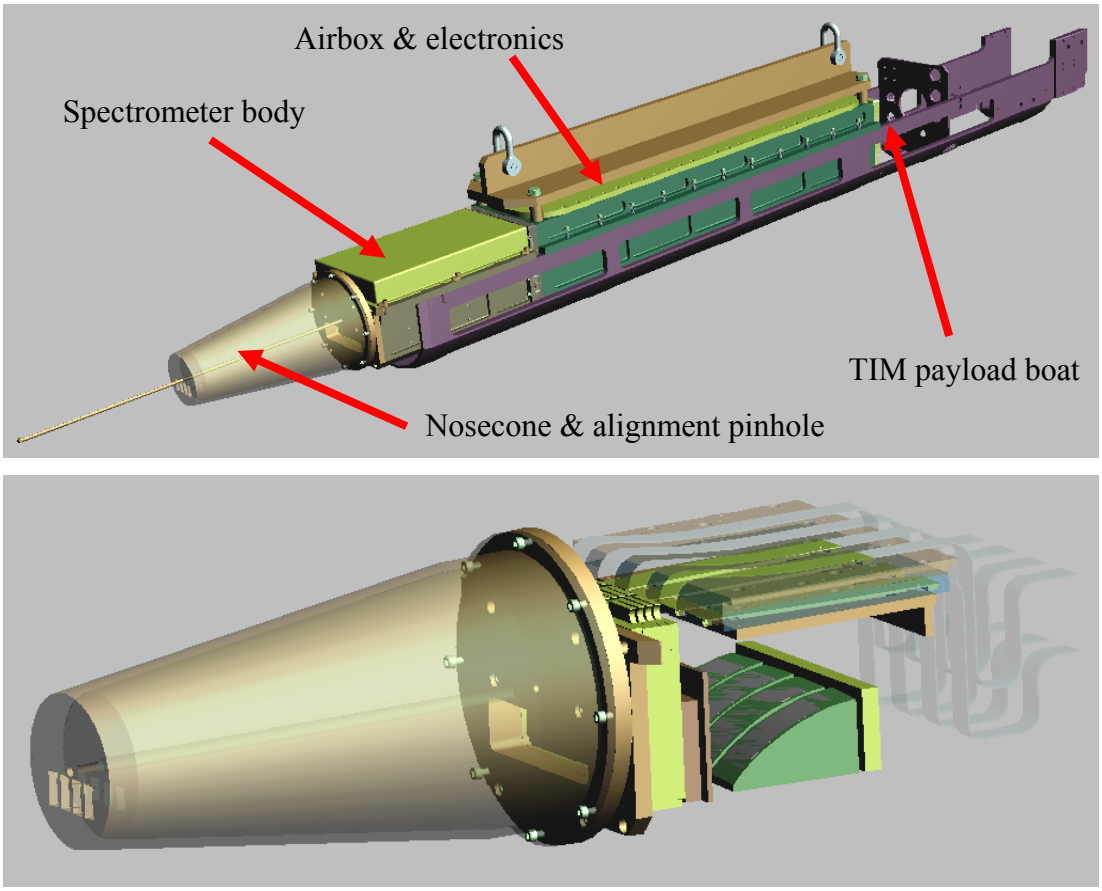

Figure 7: Latest CAD drawings of HEX-ID showing the spectrometer and airbox in a TIM payload boat (top), and a closer view of the spectrometer showing the nosecone with apertures and pinhole, the filter assembly, crystals, detector module and cabling solution (bottom).

2.1 Desirable X-ray Extraction

Various unwanted products are expected from the laser-target interaction along with the desirable soft x-rays. These include: high energy x-rays; electrons; neutrons; electromagnetic interference (EMI)/ electromagnetic pulses (EMP); and general debris. Extraction of the soft x-rays is done by using collimation and filtering as well as particle and debris removal techniques. *Figure 8* is an illustration of the key components within the spectrometer portion of the diagnostic and highlights areas to be discussed within this section.

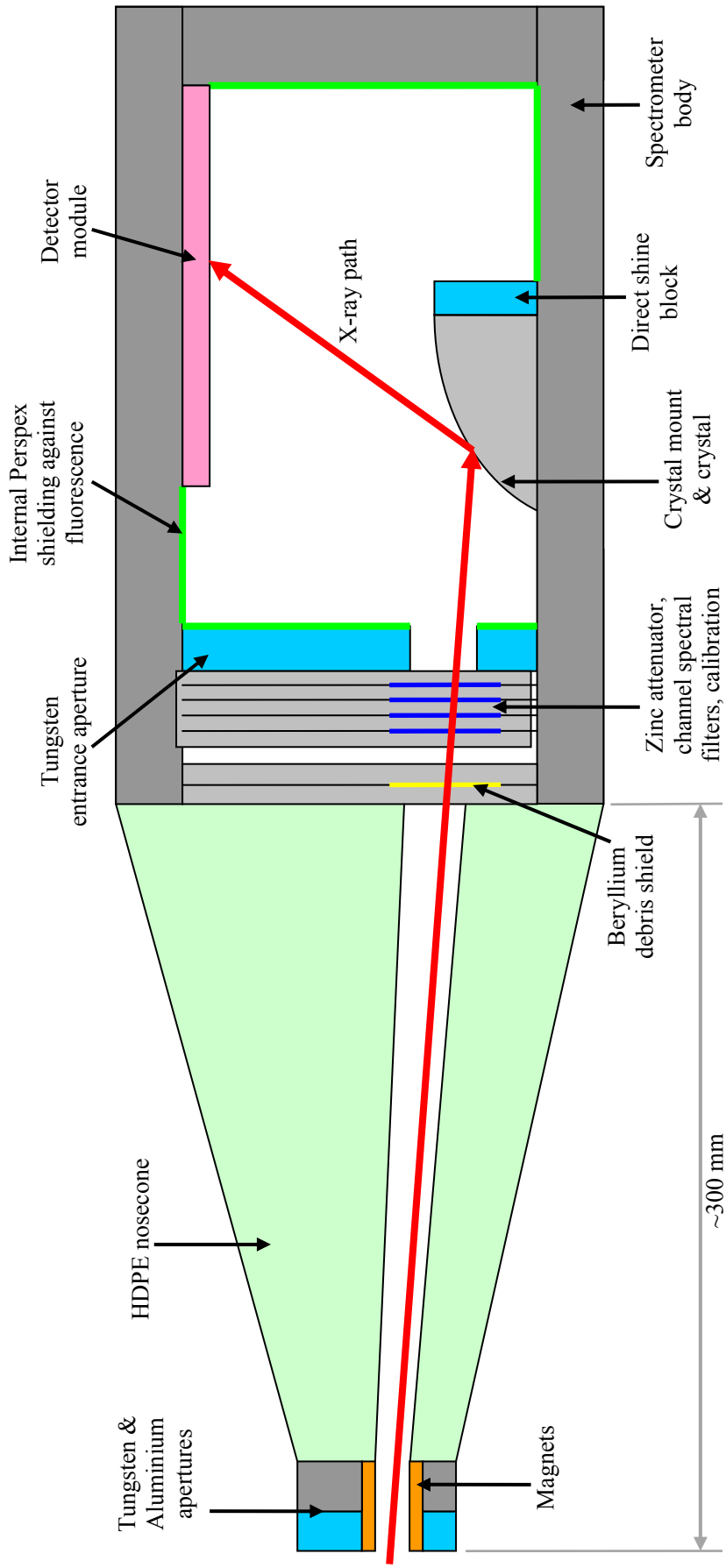

Figure 8: Schematic showing the path of x-rays through the HEX-ID diagnostic and the key components.

2.1.1 Nosecone & Magnets

A nosecone section at the front of the diagnostic will be filled with high density polyethylene (HDPE) and contain magnets at the front apertures to deflect and remove unwanted high energy particles. These will primarily be electrons originating from short-pulse interactions that HEX-ID will mainly be used to diagnose. The magnet strength necessary to deflect the high-energy electrons expected to be emitted in Orion short-pulse laser-target interactions was investigated. Sintered Rare Earth Cobalt magnets (SmCo 2:17), supplied by MMG MagDev Limited of length 19 mm, width 10 mm and height 3 mm, were selected to be positioned above and below each channel at the front of the nosecone. The opposing magnets at either side of each channel aperture produce a magnetic field strength of approximately 700 G (0.07 T) at the aperture midpoint. There were space restrictions for the overall length of the nosecone and where the magnets could be positioned so this was deemed to be the optimal set up. The maximum electron energy (E) that will be deflected in the length of the nosecone is approximately 5 MeV was calculated using *Equation 1*:

$$B = \frac{\gamma m_0 v}{re}$$

Equation 1

where: $\gamma = \frac{E}{m_0 c^2}$

B is the magnetic field strength in (T);

m_0 is the rest mass of an electron (9.11×10^{-31} kg);

v is the relativistic velocity of the electron (ms^{-1});

r is the radius of the path the electron will take when deflected by a magnetic field and is equal to the length of the nosecone (~0.27 m);

e is the charge of an electron (1.602×10^{-19} J); and

c is the speed of light (3×10^8 ms^{-1}).

2.1.2 Collimation

Collimation in the nosecone is implemented in the form of a plate of a high atomic number (Z) material, Tungsten, at the front of the nosecone, the input aperture and at the detector plane. High energy x-rays (energies significantly greater than 10 keV) will pass through the crystal and mount relatively unaffected. A 'direct shine' block of Tungsten is placed behind each of the crystal mounts to attenuate these x-rays and reduce scattering. Tungsten was the material of choice for collimation and blocking high energy x-rays as it has a high atomic number but only experiences medium activation when exposed to radiation [17]. A high power laser such as Orion has the ability to make materials radioactive as a direct or indirect result of the laser-matter interaction. This induced radioactivity is known as activation and has to be taken into account to estimate the dose personnel may receive when working in the facility.

2.1.3 Debris Shield

Debris will be blocked by a blast shield filter, in order to protect the crystals. Beryllium is the most suitable material as a debris shield as it has a low atomic number so provides good transmission to maximise spectrometer efficiency and control over signal levels through subsequent filtering. The K and L absorption edges of Beryllium will not interfere with subsequent filtering required to define the spectral ranges for the channels. Beryllium can be toxic when damaged so additional measures will be required for the handling and storage of these filters. These facilities will be in place at Orion as Beryllium is used on other diagnostics. It will be mounted on a separate filter holder in the front apertures to allow easy removal and quarantine.

2.1.4 Filtering

Following collimation, and particle and debris removal, incoming x-rays will be attenuated and filtered. Attenuators were chosen to select the range of 1 to 10 keV x-rays (zinc has an L-absorption edge at 1 keV and the K-absorption edge at

9.66 keV) and reduce the x-ray flux to a level suitable for the detectors. Edge filters have been chosen to select particular energy ranges within the 1 to 10 keV spectral range and minimise contributions outside the desired energy ranges. Collimated and filtered soft x-rays will then be incident on curved crystals. Calibration filters will mark the detector where the K-absorption edge is of that material, which can then be used to determine the other characteristic x-ray energy lines produced in a laser-plasma experiment [18].

2.1.5 Activation & Fluorescence

The body of the HEX-ID diagnostic will be made from Aluminium (approximately 1 cm thickness) in order to make it sufficiently light to load and transport as a TIM-based diagnostic. From simulations of activation of alloys expected to be within close proximity of the target at Orion, Aluminium alloys Al5083 and Al6061 would be the most suitable for the construction of the spectrometer. These generate far lower doses to personnel than Stainless Steel alloys SS304L and SS316L, the use of which should be avoided. The alloys investigated contain different percentages of elements which can be ranked in order of activation and dose from low to high: C, P, Fe, Mn, Al, Cr, Mg, S, Si, Ni, Cu, Ti, Zn and Mo. These individual elements have an effect on the activation of the overall alloy. [17]

Since Aluminium has a low atomic number, there is greater potential for scattering/fluorescence within the spectrometer. This may be minimised by using shielding on the inside of the spectrometer, including Perspex shields to absorb secondary electrons. Fluorescence from the crystals may occur if the incoming x-rays are intense and have a high energy. The selection of crystals will take this into account. Elements with a low atomic number produce less fluorescence when excited than those with a high atomic number. With x-rays above 30 keV, it is expected that scattering from the spectrometer material and the crystal mount will be more apparent than the crystals themselves [19]. Tungsten collimation on the detector modules will ensure the detector only views its crystal and not other parts of the instrument.

2.2 Crystals

Similarly to Henway and HENEX, convex reflection crystal geometry is used with HEX-ID. It has been long known that curving the crystals used in Bragg crystal spectrometers could significantly improve the performance seen [20]. Bending a crystal changes its lattice so that the angle an x-ray interacts with each plane changes as it moves through the crystal, resulting in an increase of the integrated reflectivity [21]. Convex reflection crystals disperse the x-rays along the length of the detector so increasing the spectral resolution achievable from a particular detector. The intensity of the signal is reduced somewhat compared to that of a concave crystal setup where the x-rays are focussed from a large input aperture onto a small detector area. The required energy range can be achieved solely by the divergence of the x-rays from the source if the range is not too large. If however, the required energy range is greater than the source divergence then convex crystals need to be implemented. Flat or concave crystals can be used when the required energy range is less than the divergence of x-rays from the source at the entrance aperture. [1]

HEX-ID will consist of four channels, each of which has a different convex reflection crystal, bent to a particular radius of curvature. The use of convex crystals allows a compact design to meet the size constraints of the TIM and provides necessary resolving power for the diagnostic. To allow ease of access to the detector module and have a single plane of detection, the four crystals will be positioned next to each other on the lower half of the instrument with the detectors positioned above the crystals as shown in the CAD design (*Figure 7*). The selection of appropriate crystals was based on appropriate lattice spacing, lattice orientation, elastically bendable limits, relative fluorescence and commercial availability.

2.2.1 Convex Reflection Crystal Geometry

The energy dispersion, spectral coverage of each channel and resolving power expected from HEX-ID were calculated based on the convex crystal geometry shown in *Figure 9*.

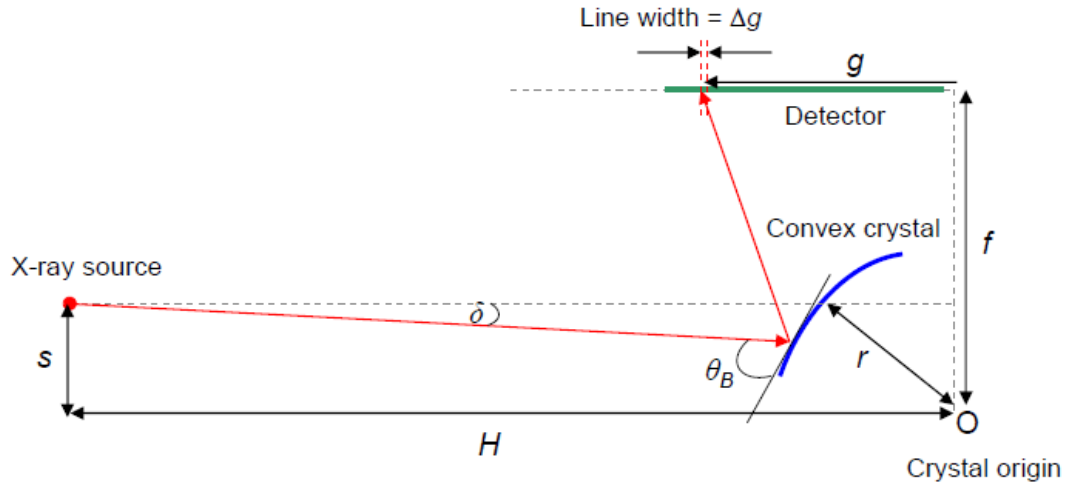

Figure 9: Schematic of the convex reflection crystal geometry utilized in the design of HEX-ID.

The energy dispersion along the detector plane, g (mm), is given by:

$$g = r\sin(\theta_B - \delta) + \frac{r\cos(\theta_B - \delta) - f}{\tan(2\theta_B - \delta)}$$

Equation 2

where: $\theta_B = \arcsin\left(\frac{hc}{2dE}\right)$; and

$$\delta = \arcsin\left[\frac{-rH\cos(\theta_B) + s\sqrt{H^2 + s^2 - r^2\cos^2(\theta_B)}}{H^2 + s^2}\right];$$

r is the radius of curvature of the crystal (mm);

f is the height of the detector above the crystal origin (mm);

H is the source to origin horizontal distance (mm);

s is the source to origin vertical distance (mm);

hc = 12.3984 keVÅ,

$2d$ is the crystal lattice spacing (Å); and

E is the x-ray energy (keV).

Positive values of g are to the left of the crystal origin in *Figure 9*, while negative values are to the right of the origin.

The resolving power, *R*, may be calculated from *Equation 2* using:

$$R \approx \frac{E}{\Delta g}\frac{dg}{dE}$$

Equation 3

where *Δg* is the spectral line width. In order to evaluate *Equation 3*, it is necessary to first reduce the complexity of *Equation 2* by making the assumptions of:

$\left(\frac{r}{H}\right)^2 << 1$ and $\left(\frac{s}{H}\right)^2 << 1$ so that: $\delta = \arcsin\left(\frac{s - r\cos\theta_B}{H}\right)$.

Calculation of these assumptions based on the parameters for HENEX noted in *Table 1* show them to be valid. Similar dimensions were used with HEX-ID so the assumptions are justified. It is then possible to compute an analytical result for the resolving power using the aid of a mathematical program such as MAPLE. The form of the resolving power used in calculations can be found in *Appendix A.2*, but it can also be represented analytically as:

$$R = \frac{E}{\Delta g}\frac{\left[-r(\cos A)(\alpha - \beta + r(\sin A)(\alpha - \beta)\right]}{\left[\tan B + (r\cos A - f)[1 - \tan(B^2)](2\alpha - \beta)\cot(B^2)\right]}$$

Equation 4

where: $A = -\arcsin(p) + \arcsin\left(\frac{\gamma}{H}\right)$;

$B = A - \arcsin(p)$;

$p = \frac{hc}{2dE}$;

$\sigma = \sqrt{4 - \left(\frac{hc}{dE}\right)^2}$;

$\alpha = \frac{hc}{(dE)^2\sigma}$;

$\beta = \frac{2rp^2}{\sigma EH\sqrt{1 - \left(\frac{\gamma}{H}\right)^2}}$; and

$\gamma = s - \frac{r\sigma}{2}$.

Based on the calculation of *Equation 3*, desirable improvements in the resolving power can be obtained by: reducing the crystal radius of curvature (r); increasing the height of the detector above the crystal origin (f); increasing the source to origin vertical distance (s); and reducing the spectral line width (Δg). Calculations of the potential energy dispersion, spectral range and the resolving power for HEX-ID were performed using the parameters of HENEX as a basis (*Table 1*). The parameters H, Δg and s were held constant, while the values of f and r were adjusted for a variety of crystal lattice spacings. The desired characteristics were obtained by allowing the detector plane to have two positions, to optimise spectral range or resolving power, and by selecting a minimum radius of curvature for the crystals, which was ultimately constrained by how far the crystal could be bent before fracture. Exact values for H and s are fixed and resulted from the size of the spectrometer nosecone, the positioning of the crystals within the instrument and the fielding of the instrument at Orion. The parameter Δg is dependent on the detector used and the x-ray energy recorded.

Parameter	HENEX	HEX-ID
Radius of curvature, r (mm)	127	117
Source to origin horizontal distance, H (mm)	584.7	709
Source to origin vertical distance, s (mm)	94.7674	135
Height of sensor above origin, f (mm)	138	139.2 and 166.2
Spectral line width, Δg (μm)	-	100

Table 1: Selected parameter values initially used in calculations match those of HENEX and the final values of parameters for HEX-ID are detailed.

A plot of g versus E is shown in *Figure 10*, while R versus E is shown in *Figure 11*. Both graphs are shown at the two limits for the crystal to detector separation, illustrating the expected variation in spectral range and resolving power. The characteristics for each channel, and the final crystal selection, are summarised in *Table 2*.

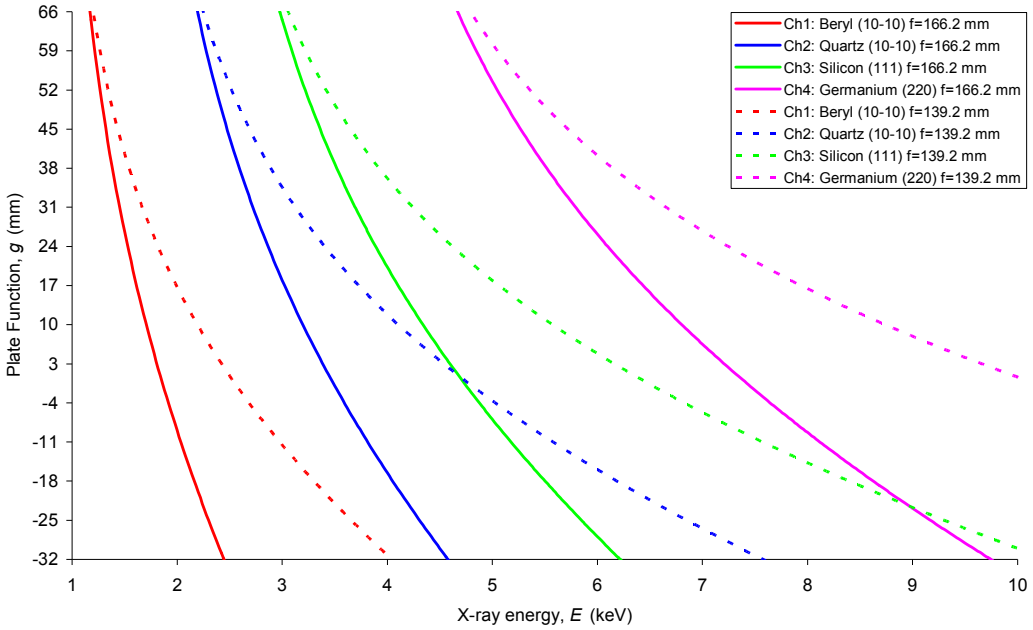

Figure 10: Energy dispersion and spectral range expected for each of the four channels. The crystals and reflection planes used are: Beryl (10-10), Quartz (10-10), Silicon (111) and Germanium (220). The two heights of the detectors above the crystals give separate ranges as shown with solid and dashed lines.

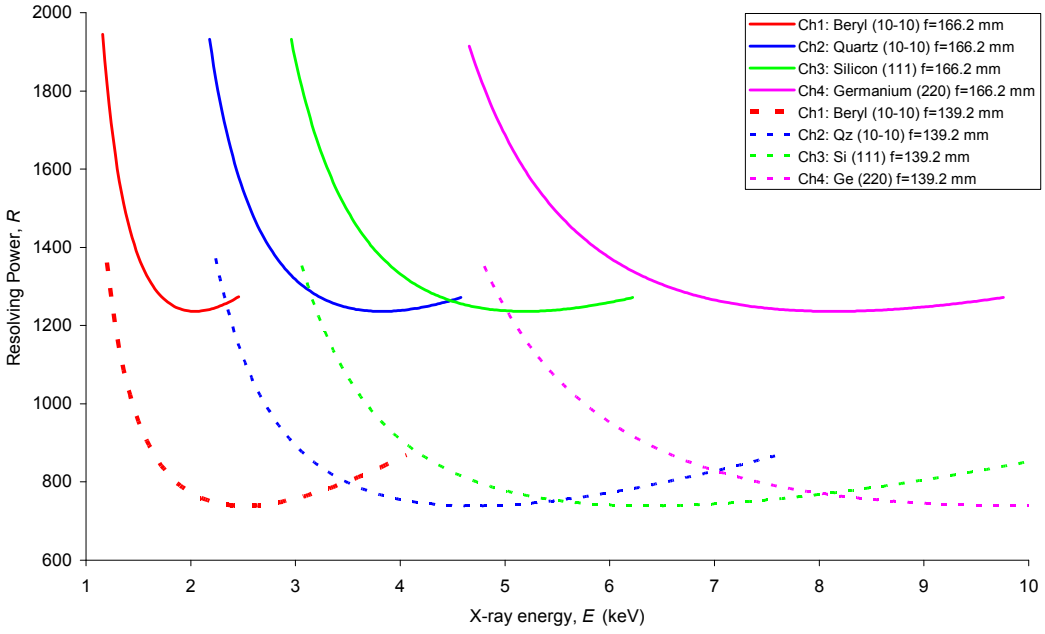

Figure 11: Resolving power obtained from each of the four channels assuming a minimum detector spatial resolution $\Delta g = 100$ μm. The two heights of the detectors above the crystals give separate ranges of R as shown with solid and dashed lines.

Channel	1	2	3	4
Crystal & plane	Beryl (10-10)	Quartz (10-10)	Silicon (111)	Germanium (220)
Thickness (μm)	85	100	100	100
Lattice spacing, *2d* (Å)	15.95	8.514	6.272	4.00
Plate function, *g* (mm)	66 to -32			
Energy range at *f*=139.2 & 166.2 mm (keV)	1.2 to 4.0 1.2 to 2.5	2.3 to 7.6 2.2 to 4.6	3.1 to 10.3 3.0 to 6.3	4.8 to 16.1 4.7 to 9.8
Bragg angle at *f*=139.2 & 166.2 mm, θ_B (°)	40.1 to 11.1 41.4 to 18.5			
Theoretical resolving power (max to min)	1361 to 738 2000 to 1237	1372 to 738 1896 to 1236	1353 to 738 2000 to 1236	1352 to 738 1967 to 1236

Table 2: Crystal selection for HEX-ID and relevant parameters. The calculated performance characteristics for each channel are also included.

The spectral range from 1.2 to 9.8 keV is obtained when the *f* value is set to its maximum (166.2 mm), which achieves a theoretical resolving power of ~1200. Using the minimum *f* value (139.2 mm) will allow a similar spectral range to be obtained for two types of detector fielded simultaneously, each occupying half of the active area, although from *Equation 2*, the resolving power is reduced to ~730. The front half of the detector plane will capture 1.2 to 8.3 keV with a small gap between 2 and 2.2 keV, while the rear half will capture 2 to 9.8 keV.

Line width (Δg) in the geometry calculations takes into account spectral line broadening resulting from blur due to the crystal, source and detector. Line broadening is contributed to by a number of factors including: detector broadening, source broadening, crystal thickness, natural widths of the x-ray transitions, crystal

rocking curve width, geometrical aberrations. [22] Additional contributions of Doppler (thermal motion of radiating atomic systems) and Stark broadening may result if the x-ray source is a laser-produced plasma. Large plasmas can produce opacity broadening and the effective resolving power decreases with source size increasing. The self-absorption occurring in large, dense plasmas could result in a severe dip in the spectral line causing confusion as to whether there are two lines or not. [23]

2.2.2 Crystal Mounts

An Aluminium crystal mount was designed and fabricated to the correct radius of curvature, which would allow the crystal to be glued in position. Threaded holes have been included in the mounts to attach them to the spectrometer body. *Figure 12* shows all four crystals glued onto the mounts in the order they will be positioned in the spectrometer. The crystals can be inspected between laser shots by looking down on top of them with the detector module removed. If damage is noted then the instrument will have to be removed from the TIM to replace the crystal.

A crystal thickness of approximately 200 μm was decided upon as it would provide good transmission of high energies (>30 keV), it could be bent to the desired radius of curvature, and minimising crystal thickness can reduce line broadening. Past experience with HENEX also indicated reasonable x-ray intensity for reflected x-rays if there was sufficient thickness of material. The actual thickness of each crystal was decided by the crystal manufacturer (Saint-Gobain Crystals) to meet the requirements for the bending process. The crystals were of length 65 mm and width 25 mm.

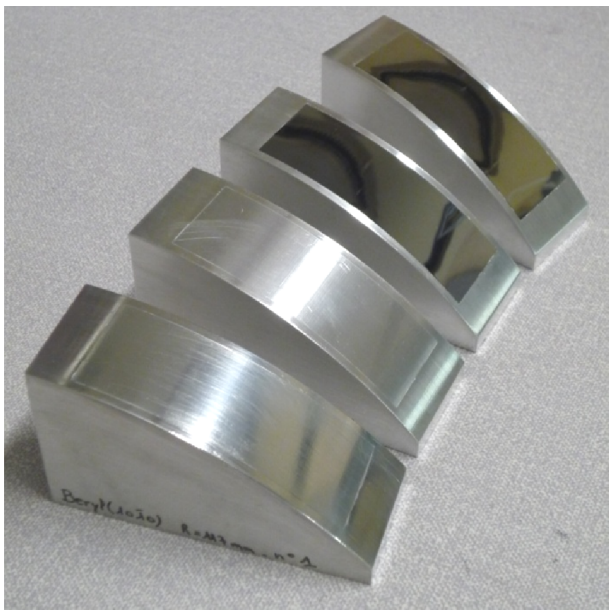

Figure 12: Photo of the four crystals glued on their mounts after characterisation had taken place. The order from bottom left to top right is Beryl (10-10), Quartz (10-10), Silicon (111) and Germanium (220).

2.3 Detection System

Time-integrating and time-resolving x-ray detectors are required for HEX-ID. They must be sensitive to x-rays in the region of 1 to 10 keV and must provide very high resolution to provide enhanced identification of characteristic x-ray line emissions. Various detectors were investigated for suitability, allowing the active area of detection of each channel (~100 mm by ~25 mm) to be covered.

2.3.1 Detector Modules

Based on detector spatial resolution, cost, availability of space to be able to move the detector plane (to control resolving power and spectral range), detector sensitivity and problems associated with an electromagnetic pulse environment, the different detectors that will be used in HEX-ID are: Fuji BAS TR image plate (IP); Rad-icon Imaging Corporation Radeye 1 CMOS sensors; and Alameda Applied Sciences Corporation Diamond Radiation Detectors (PCD) (*Figure 13*).

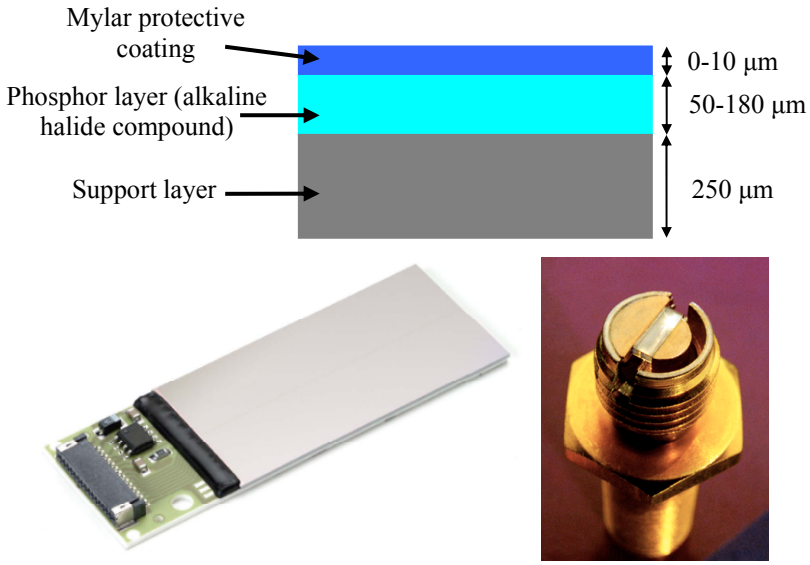

Figure 13: (Top) typical layer structure and composition of an IP. (Bottom left) photograph of the Rad-Icon Radeye 1 CMOS sensor [24]. (Bottom right) photograph showing a PCD with the diamond element mounted within an SMA connector [25].

IP is reusable 2D sheet that serves as a detector of ionising radiation. The typical composition of an IP is shown in *Figure 13*. Incident x-rays are absorbed by photosensitive phosphor that creates F-centres (electron trapped in an anion vacancy). By this method, the x-ray image is stored in the IP. An IP scanner is used to recover the image from the exposed IP by irradiating the IP with laser light which excites trapped photoelectrons. This photo-stimulated luminescence (PSL) can be detected by a photo-multiplier tube (PMT) and recorded on the computer system. The IP can be then erased using a bright light for a few minutes allowing the IP to be reused. [26] IP has many advantages over other x-ray detectors which include high sensitivity, wide dynamic range, low signal-to-noise ratio, and the linearity and uniformity of the response. IP can be bent into different shapes and cut to a desired size, and is immune to damage or interference that can be induced by an electromagnetic pulse (EMP) environment. [27] IP will provide time-integrated data where the energy dispersion and spectral range are more important considerations than resolution achievable, such as during commissioning tests. It can also be used to make relative comparisons of line emissions on the same piece of image plate for a given laser shot.

CMOS sensors are matrix-addressed photodiode arrays. The Radeye 1 is a 2.5 cm by 5 cm, 512 by 1024 pixel CMOS detector with all support and control functions integrated on-chip to minimize the amount of external circuitry needed to run the imager. [28] The CMOS sensors were chosen over Charge Coupled Devices (CCD) because: they are much cheaper than producing a custom CCD; they are more compact; they do not require a cooling system; and can provide a similar resolution. Although the dynamic range is smaller than for image plate (85 dB compared to >100 dB), the sensor has higher quantum efficiency and due to it being electronic, there is no additional processing time to record the data following a laser shot.

The PCD detectors to be used consist of a diamond element mounted in a SMA vacuum feed-through. Radiation generates electron-hole pairs within the diamond [29]. There is a linear dependence between the resistance of a PCD and the power of the incident x-ray photon as well as the bias voltage applied to the system [30]. They are suitable for x-ray detection up to 10 keV due to the low atomic number of diamond [31]. PCD detectors are rugged, radiation hardened, and have very fast time response due to the short electron-hole recombination time [30]. PCD detectors will allow the temporal evolution of the x-ray flux in the energy range within each channel to be recorded with a time resolution of 0.3 ns [31]. The Radiation Science Group at AWE currently uses these detectors for their experimental programme.

The ability to change the type of detectors in use will be a key asset of this diagnostic. Simple removal and insertion of each detector is the best option and allows for various combinations of the three devices to be used. Using a selection of detectors also provides HEX-ID with a very large dynamic range. Since the detectors chosen vary significantly in size and shape, it is necessary to have different detector modules. Six separate detector modules will be designed to deliver all experimental requirements:

1. A single piece of image plate spanning all four channels, held within a cassette for transport. This allows a single intensity comparison and verification of the energy dispersion for setup purposes.

2. An array of eight CMOS sensors. To achieve the length required to record the energy dispersion, two sensors will be placed head-to-head with a minimal gap between them at the joint.
3. A single piece of image plate covering half of each channel combined with four CMOS sensors. The IP will be placed towards the front of the instrument with the CMOS sensors to the rear to allow for easier positioning and removal of the IP without obstruction from wiring.
4. A single piece of image plate covering half of each channel combined with four PCD detectors, one in each channel. The PCDs are to be moveable to align with particular characteristic energies. The IP will be placed towards the front of the instrument with the PCDs to the rear, again for ease-of-access reasons.
5. Four CMOS sensors combined with a PCD array, each occupying half the module. This module will be used to maximise the spectral range while providing enhanced spectral (CMOS) and temporal (PCD) information from the same laser-plasma interaction. The CMOS sensors will be positioned towards the front of the spectrometer with the PCDs towards the rear.
6. This module is the same as "Module 5" except the CMOS is towards the rear of the spectrometer and the PCDs towards the front.

Any one of these modules can be easily inserted from the top of the diagnostic prior to a laser shot (*Figure 14*). This top-loading will allow easy access to the electronic detectors if they require repair, or removal of the image plate cassette for scanning after a shot. The detector module design will depend on the method of detection and must account for constraints in moving the plane of detection to achieve improved resolving power or spectral coverage.

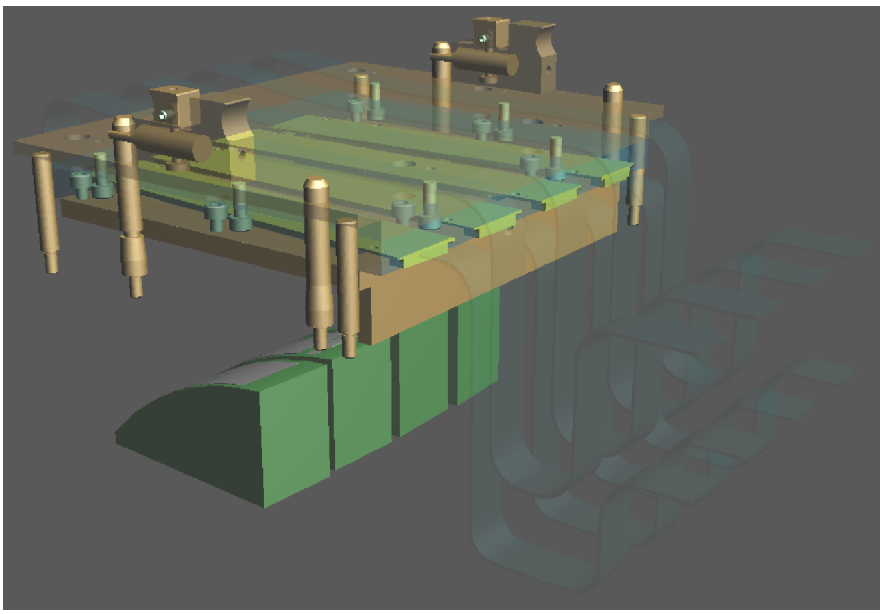

Figure 14: CAD drawing of the CMOS detector module in position above the crystals, and the alignment pins and retaining clips to hold the various modules in place.

2.3.2 Electronics System

Fielding the electronic sensors (CMOS and PCD) requires hardware, cabling and software that the IP does not. They require power inside the TIM and a way to export the data they obtain so it can be recorded and viewed. The Orion TIM bulkhead has the connections shown in *Figure 15*. Upon analysis of the wiring required to operate the electronic detectors, it was realised that the existing bulkhead connections would not be adequate. Options investigated to meet the requirements included: changing the TIM bulkhead to give more connections when the instrument is used; mounting the instrument on a non-TIM port; only using IP as the recording media and not electronic sensors; or developing a processing and storage unit to sit inside the TIM with the spectrometer which would process the information from the detectors and relay it through the existing TIM bulkhead connections to the Target Data Acquisition System (TDAS).

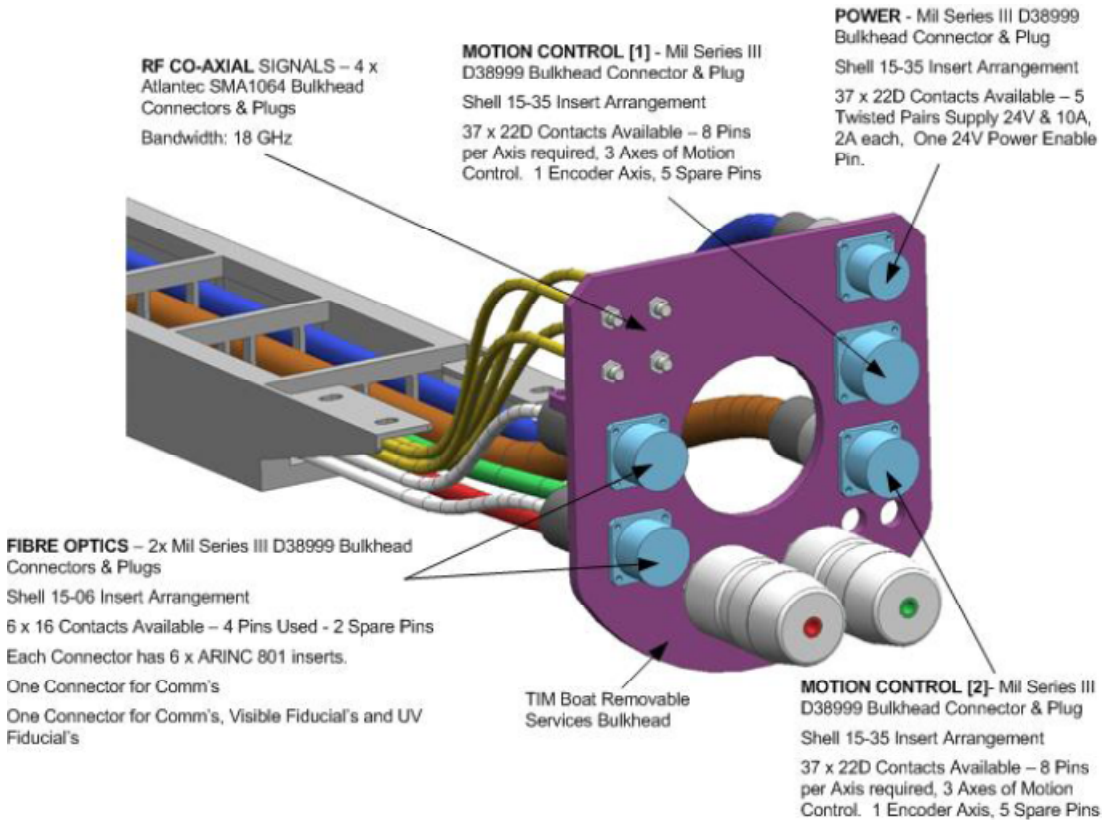

Figure 15: The available connections and layout of the TIM bulkhead, as it would appear looking from inside the chamber outwards. [32]

It was decided to source a processing unit which would be contained within an airbox behind the spectrometer in the TIM which would meet the CMOS sensor requirements. The excessive cost of changing the TIM bulkhead and running new cables to all TIMs that HEX-ID may be fielded in prevented that option. Using only IP or fitting HEX-ID to a non-TIM port, were excluded as options due to not meeting the original user requirements. This processing unit will make use of the 24 V power supplied as standard to the TIM and the fibre optic connections on the TIM bulkhead to export captured data. A CompactRIO (cRIO) platform from National Instruments (*Figure 16*) has dimensions suitable for housing the TIM. A cRIO system has field-programmable gate array (FPGA) technology within the chassis, a real-time processing unit and a selection of input/output modules. The software required to operate the cRIO is written within the graphical program LabView. The complete system can provide the processing power needed to control up to eight CMOS sensors with a suitable selection of modules (*Table 3*). Specific features and parameters of each module can be found on the National Instruments website [33].

Figure 16: Photo of the National Instruments CompactRIO chassis, controller and some of the selected modules.

Product name	Description	Quantity
cRIO-9116	8-slot cRIO chassis	1
cRIO-9025	Real-time PowerPC embedded controller	1
NI 9401	8-channel TTL digital input/output module: CLOCK – 1 MHz signal to read each pixel START – ½ Hz signal to read the sensor every 2 seconds FRAME – read frame sync out from the sensor	3
NI 9402	4-channel TTL digital input/output module: Input from Orion in form of ½ Hz trigger and shot trigger	1
NI 9485	8-channel relay: Switches on/off 5 V and 3.8 V supply to each sensor	1
NI 9227	4-channel current input module: Measures the current draw through 5 V and 3.8 V supplies	1
NI 9223	4-channel analogue to digital converter: OUTS & OUTR – receives data from sensor	2

Table 3: Specifications of the CompactRIO chassis, controller and modules chosen for use with the CMOS sensors.

Figure 17 shows an overview of the key electronic components required within the TIM to operate the spectrometer. The 24 V supply within the TIM will be converted to provide each CMOS with the 5 V and 3.8 V they require, and provide the appropriate power to the other electronic components. The data from the sensors will be temporarily saved on the cRIO, to be downloaded after the shot through the TIM bulkhead via the Ethernet connection and media converter. Two SMA connections on the bulkhead will provide the cRIO with clock pulses to trigger the data recording as the laser shot is fired. Remote switches will be used to switch the cRIO and laser pointer on and off when required. LabView software has been written to communicate with the cRIO while it is housed in the airbox. A test box will be constructed to evaluate the software for control of four sensors. The wiring diagram for this can be found in *Appendix A.3*.

The PCDs require a high voltage (~300 V) bias to be supplied to the SMA cables connecting the detectors to a fast oscilloscope. The four PCDs will have the signals combined into two cables for extraction from the TIM through two of the SMA connectors on the TIM bulkhead. A time delay in two of the signals will allow this, which can then be reversed once past the TIM bulkhead. Approximately one foot of cable is required for every 1.5 ns of delay. An oscilloscope is required to display the PCD signals. To achieve the expected maximum PCD resolution of 300 ps, an oscilloscope of at least 5 GHz will be required. Usually the x-ray pulse will be of a similar timescale to the laser pulse used to create the plasma [4]. With the duration of long pulse beams on Orion being of the order of a nanosecond, the temporal resolution of the PCDs will provide useful information. Plasmas produced from very short pulse lasers may result in x-ray pulses significantly longer than the laser pulse, perhaps in the order of tens of ps. In this case the PCD temporal resolution may not be adequate.

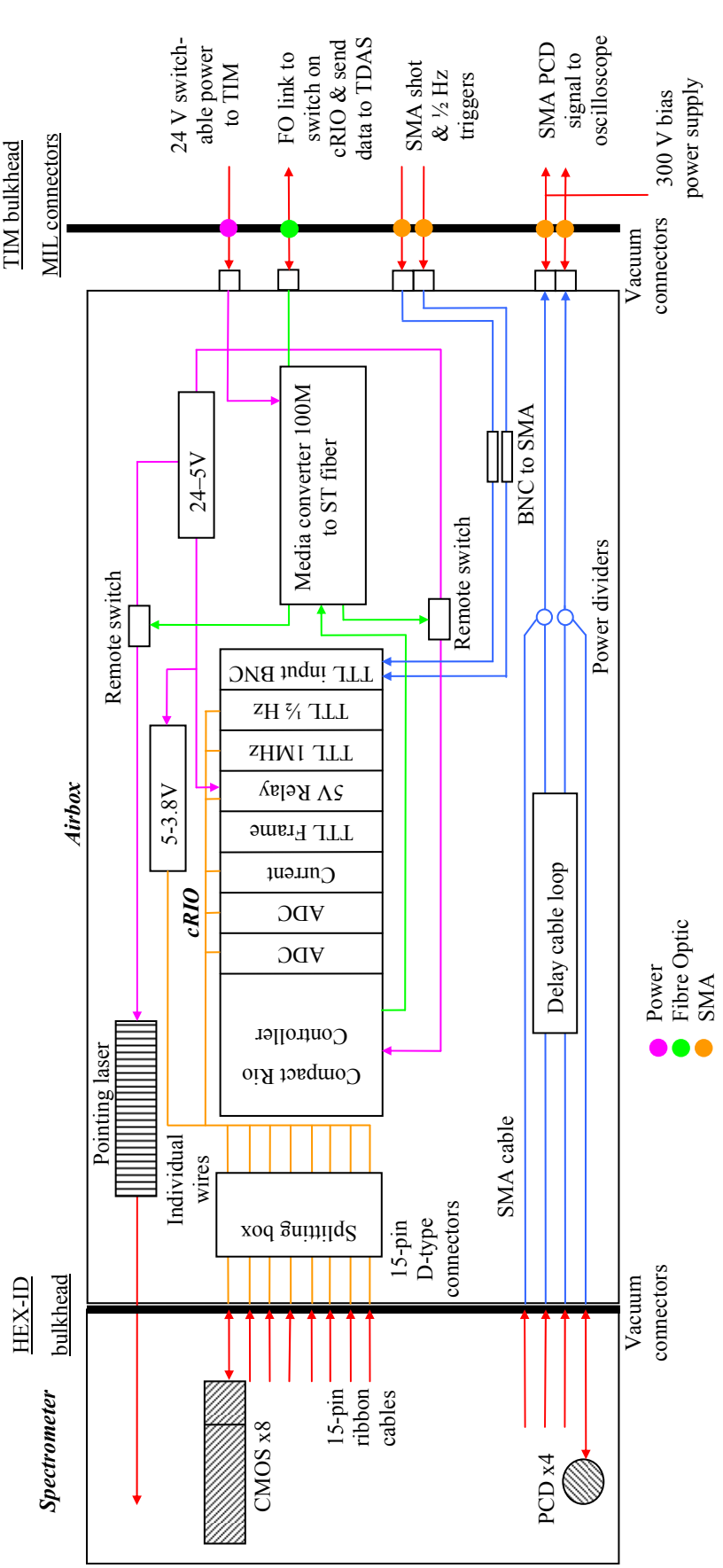

Figure 17: Diagram of all electrical components required within the TIM and within the airbox for the diagnostic to function as required. The TIM bulkhead connections being utilised are shown.

2.3.3 Characteristic X-ray Line Positions

Typically, it is expected that Kα emission will be observed from the laser-target interaction depending on target fielded. Identifiable $K\alpha_1$ x-ray lines within the spectral range of the HEX-ID diagnostic (1 to 10 keV) and are shown in *Figure 18*. This is the position that the PCD detectors will need to be placed in order to detect the temporal information of a characteristic line energy. Calibration will be required using image plate to determine where the particular energies appear and then a scale can be manufactured and attached to the PCD detector modules. The PCD can be aligned with a desired line-energy and the module inserted into the instrument. Depending on the height of the detector module, two scales will be required highlighting the various energies.

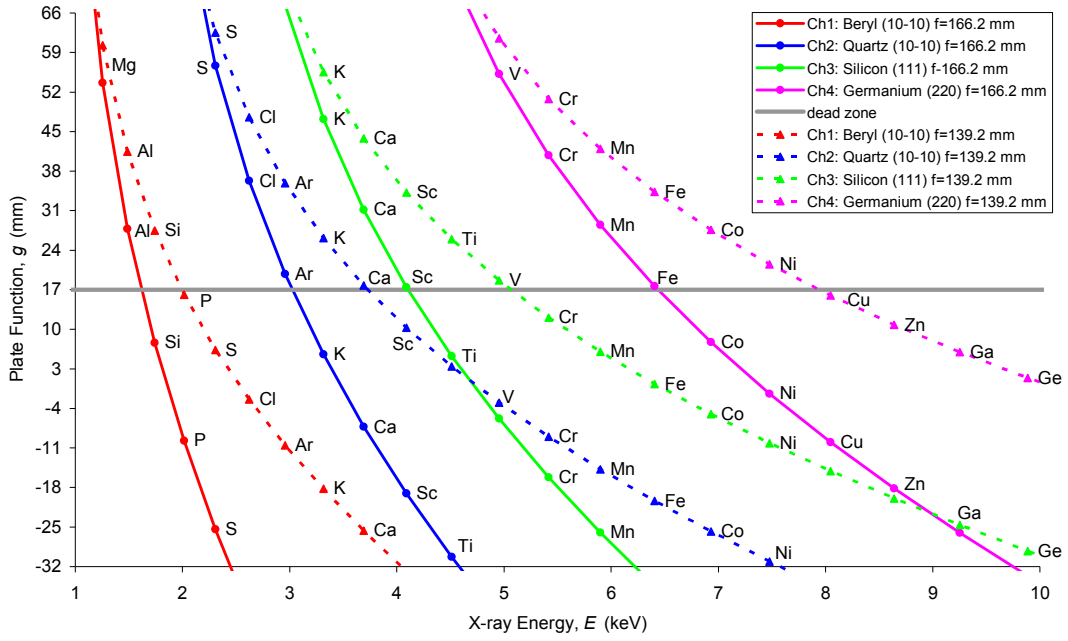

Figure 18: $K\alpha_1$ characteristic x-ray line positions along the length of each channel. The dead zone at the joint between two CMOS detectors is represented.

At the joint between two CMOS sensors there will be a dead zone of approximately 100 µm where no pixels exist to detect the spectral lines. This is due to a 50 µm border zone surrounding the active area of each sensor [24]. With the exception of the single piece of IP, this will occur on the all other modules as the different types

of detectors cannot be joined closely. Examination of the spectral line positions reveals that some characteristic lines will fall on this dead zone with the detector module at a particular height. Fortunately, this affected line will be in a different position at the other detector height or using an adjacent channel.

2.4 Electromagnetic Pulse Shielding

Electromagnetic interference (EMI)/ electromagnetic pulse (EMP) protection is required for the electronic components utilised in the design of HEX-ID. EMP is one of the results of the interaction of a high power laser with a target. Electrons are ejected from the target and can charge one side of the target chamber, if they are ejected mainly in a single direction, causing the chamber to ring at its natural frequency. [34] The EMP level depends on the number of ejected electrons, which principally depends on the size of the target, their energy and the duration of the laser pulse [35]. Laser plasma interactions from long-pulse lasers can result in hot electrons in the range of 10 to 100 keV. A few of these electrons escape, which is thought to be the source of the EMP. Short-pulse lasers produce MeV electrons with a great deal more escaping due to their high energy. This however, is still a very small number of the total electrons produced, but the shorter duration causes a very large EMP. [36] Diagnostics can be affected in a number of ways by the electric and magnetic fields produced. This can range from a loss in signal quality or severe damage to electronic components. [37]

The EMP expected from the Orion laser has been determined from experiments with the Vulcan Petawatt laser at the Rutherford Appleton Laboratory (RAL) [34]. The resonant frequency of the Orion target chamber was calculated to be 65 MHz. The maximum E-field at the target chamber centre was calculated to be in the region of 6.98 kVm^{-1}, and the maximum H-field at the edge of the chamber was estimated to be 11.8 Am^{-1}.

Shielding for this EMP will be implemented by covering the entire instrument (including the nosecone) in an Aluminium skin, which will act as the Faraday cage to

block external electric fields. A Faraday cage is an enclosure formed by a solid or mesh conducting material, which will block external electric fields. EM waves are restricted passing through holes that are less than a wavelength in diameter. There is a cut-off frequency above which a mesh will fail to protect from EM waves. Measurements on other facilities have seen frequencies greater than 5 GHz [35, 38]. This equates to a wavelength of 6 cm and to be sure that this signal will be blocked, any holes need to be 6 mm or less. Good contact between any access panels and the rest of the instruments will be required to prevent breaks in the shield. There is no relationship between the thickness of the skin and the EMP shielding it will provide. The skin thickness was decided upon to provide structural stability and protection for components inside, but not weigh too much. The filters will block EMP signals through the apertures as they will be conductive to the rest of the spectrometer, and EMP shielded cables will be utilized to prevent external wiring providing a route into the enclosure for EMP.

2.5 Expected Signal

An intensity spectrum of x-rays produced from an Aluminium target over a range of energies from 1 to 100 keV, with a 250 ps laser pulse [39] at the Naval Research Laboratory (NRL) facility, was used as a starting point to determine the signal level expected to be produced at Orion and OMEGA EP. The intensity was converted to the number of signal electrons expected per pixel on the CMOS detectors. The assumption that the x-ray flux scales with $I\lambda^2$ was made and a scaling factor (*Table 4)* was calculated for Orion and OMEGA EP.

Facility	Intensity (W/cm^2)	Wavelength (nm)	$I\lambda^2$ ($W/cm^2/um^2$)	Scale factor
NRL	$4.00x10^{15}$	1060	$4.49x10^{21}$	1
Orion	$1.00x10^{21}$	1053	$1.12x10^{27}$	247000
OMEGA EP	$2.00x10^{20}$	1053	$2.22x10^{26}$	49300

Table 4: Scaling factors calculated for the Orion and OMEGA laser facilities based on a spectrum obtained from the NRL facility.

For a sample spectrum it has been reported that 30% of the radiated energy is emitted as characteristic lines, 60% as recombination continuum and 10% as Bremsstrahlung [40]. There are numerous papers on the intensity of emission from various individual x-ray lines within the range of interest for HEX-ID [4, 41, 42] and higher energies [43, 44]. The yield of Kα is shown to increase up to a laser intensity of $5x10^{-7}$ W/cm^2 and remain relatively constant after that [45]. It is therefore safe to assume that with the intensity of the Orion laser being above this, the yield will be great enough. Using the information found in these papers, calculations could be performed into the expected intensity for individual characteristic x-ray emission lines at the detector plane. A general spectrum was calculated for Orion and OMEGA EP from 1 to 10 keV using the intensity spectrum seen at NRL and the scaling factors detailed above (*Figure 19*).

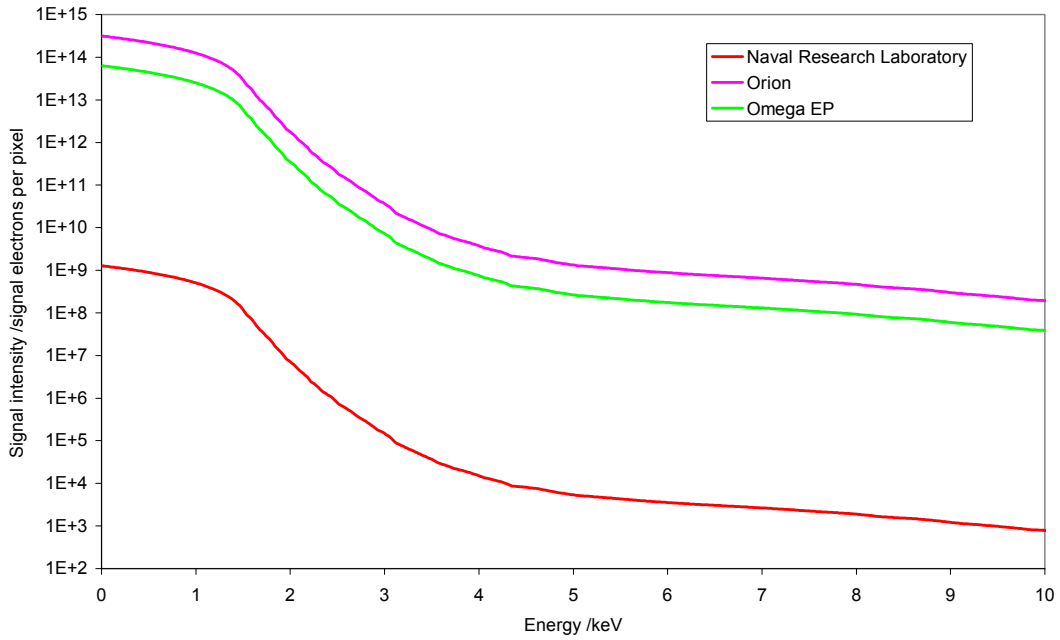

Figure 19: Expected signal intensity on the CMOS sensors for Orion and OMEGA EP extrapolated from the signal seen at the Naval Research Laboratory [39].

The signal intensity seen at the detector is affected by a number of factors as the x-rays pass through the instrument including: attenuation by filter materials; reflectivity of crystals; and quantum efficiency of the detectors.

2.5.1 Orion Signal

A schematic of the filter assembly is shown in *Figure 20*, which can house up to five separate filter materials. Before deployment of HEX-ID, the appropriate cut-off filter will be selected based on the crystal to detector separation (*f* distance). There is a need to maximise the filter thicknesses to make the filters easier to handle and position in the spectrometer, but thicker filters will reduce the signal level.

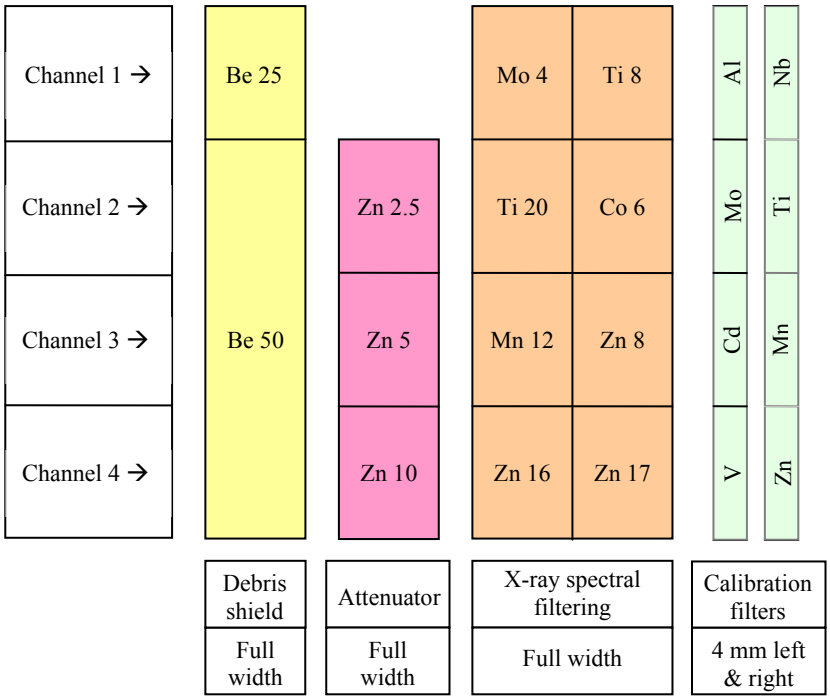

Figure 20: Filter selection expected to be used for Orion laser shots. The x-ray spectral filters will be chosen prior to a shot based on the height position of the detector module.

Since the HEX-ID crystals and detectors were not fully characterised at this stage, the crystal reflectivity was estimated to be 0.0021 at a Bragg angle of 22° [8] and the CMOS, PCD and IP quantum efficiencies were taken as 30% [46], 20% [47] and 8% [26] respectively. The calculated signal for each channel is shown in *Figure 21*, for the case of the CMOS sensors. Saturation of each pixel was noted to be 2,8000,00 electrons and the minimum dark current expected is approximately

890 electrons/pixel [24]. The reflectivity measurements detailed in *Section 3.2* will be used to improve the accuracy of these calculations before final selection.

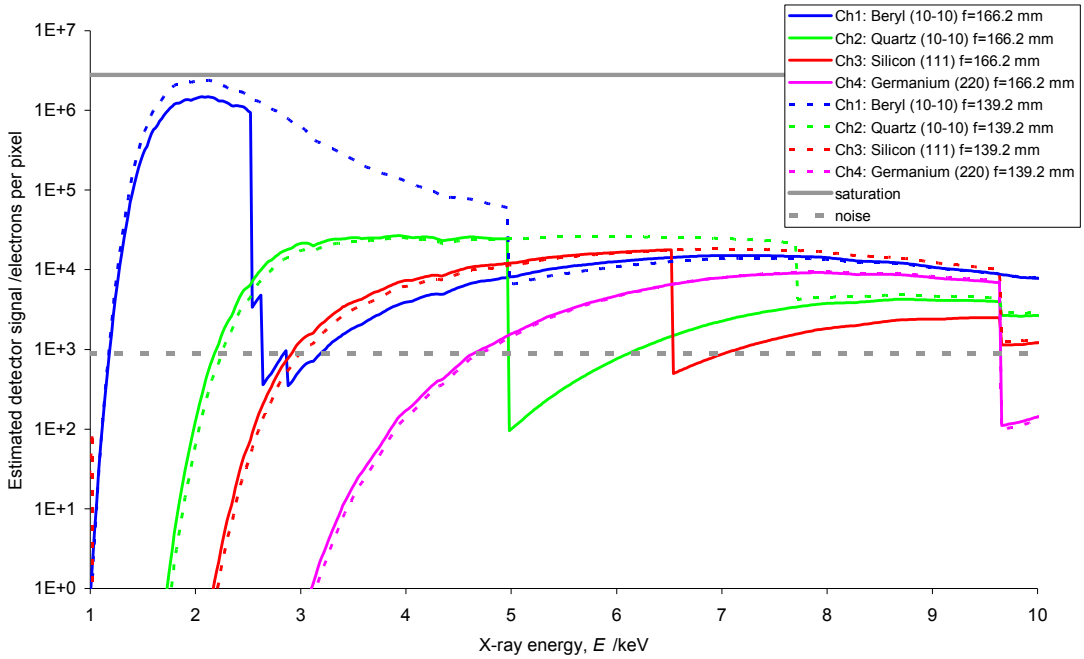

Figure 21: Orion laser facility predicted number of signal electrons per pixel for CMOS sensor with detector module in two height positions. The saturation level and noise level for the CMOS sensors are shown.

2.5.2 OMEGA EP Signal

Similar calculations have been carried out for the OMEGA EP facility to predict the thicknesses of materials that need to be inserted prior to a laser shot. *Figure 22* gives the filter materials and thicknesses selected, and *Figure 23* shows the signal levels over the entire energy range of HEX-ID.

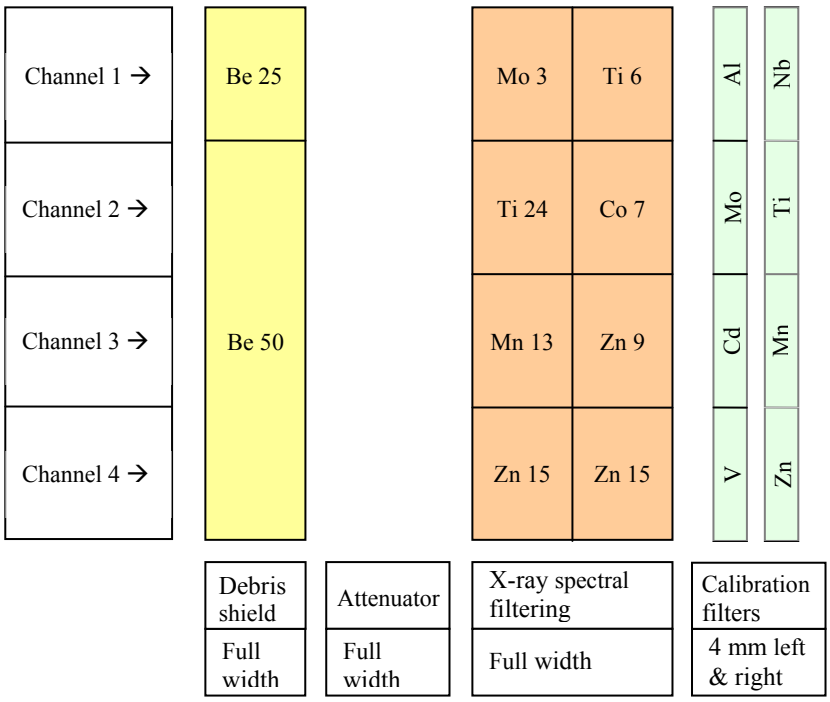

Figure 22: Filter selection expected to be used for OMEGA EP laser shots. The x-ray spectral filters will be chosen prior to a shot based on the detector height.

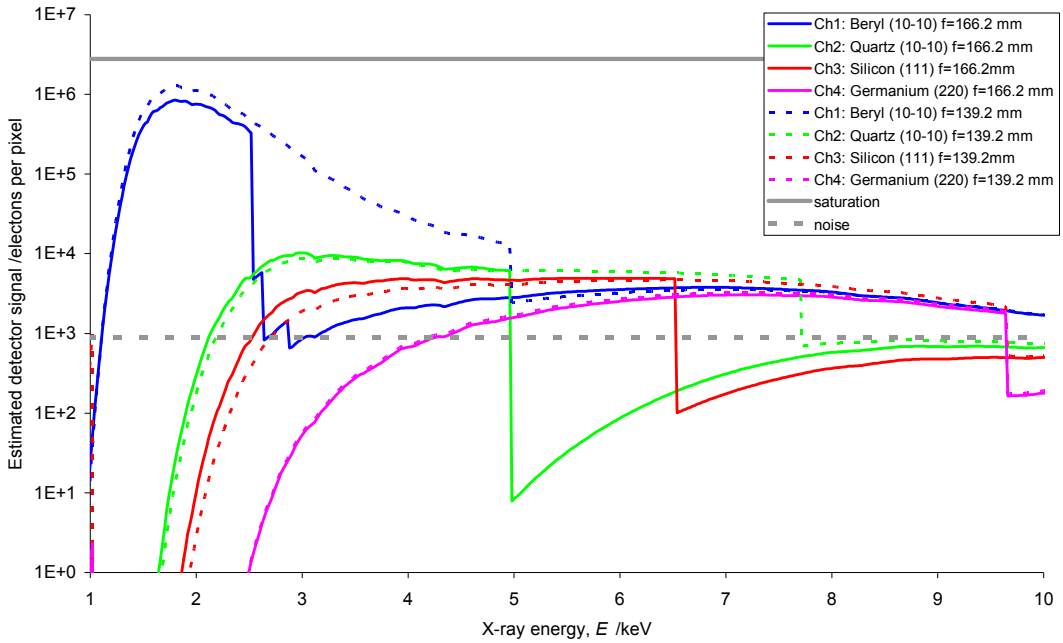

Figure 23: OMEGA EP laser facility predicted number of signal electrons per pixel for CMOS sensor with detector module in two height positions. The saturation level and noise level for the CMOS sensors are shown.

2.6 Additional Design Considerations

Several other areas of the design required attention in order to meet the user requirements such as: the method for aligning the diagnostic with the target prior to a shot; the Orion target chamber port that would be used for fielding HEX-ID; the vacuum compatibility of the finished design; and the overall mass of the diagnostic and whether it would meet the TIM specifications.

2.6.1 Pointing of HEX-ID

A small laser system and pinhole will be implemented in the design to enable HEX-ID to be accurately pointed at the target. A detachable pointer on the end of the nosecone was considered but would require retraction of the diagnostic within the TIM to remove the pointer before returning HEX-ID to its desired position. This was deemed too difficult with the limited space inside the TIM and there was a risk of damage to the target during alignment. The laser pointer method also allows alignment while the target chamber and TIMs are under vacuum. While pumping down the target chamber to vacuum, there is some movement of the TIMs and target diagnostics. Adjustment accuracy will be determined from the accuracy of the TIM movements when the instrument is fielded on Orion. The pinhole through the centre of the instrument should allow for very accurate pointing of the HEX-ID and airbox package offline. The laser (class 1 or 2) will be housed within the airbox shining along the pinhole. A diffractive lens at the end of the nosecone will produce a crosshair to illuminate the target, approximately 30 cm from the end of the nosecone. If any misalignment is evident once the HEX-ID and airbox are loaded into the TIM payload boat, the TIM actuators can then be used to correct alignment with respect to the target. After alignment the laser can be remotely switched off.

2.6.2 Orion Port Allocation

Many diagnostics are deployed using a Ten-Inch Manipulator (TIM). It allows the diagnostics to be inserted without breaking the target chamber vacuum as there is gate valve between the chamber and the TIM. *Figure 24* shows a CAD drawing of a TIM attached to the target chamber. Key components are labelled with an example diagnostic outlined for reference.

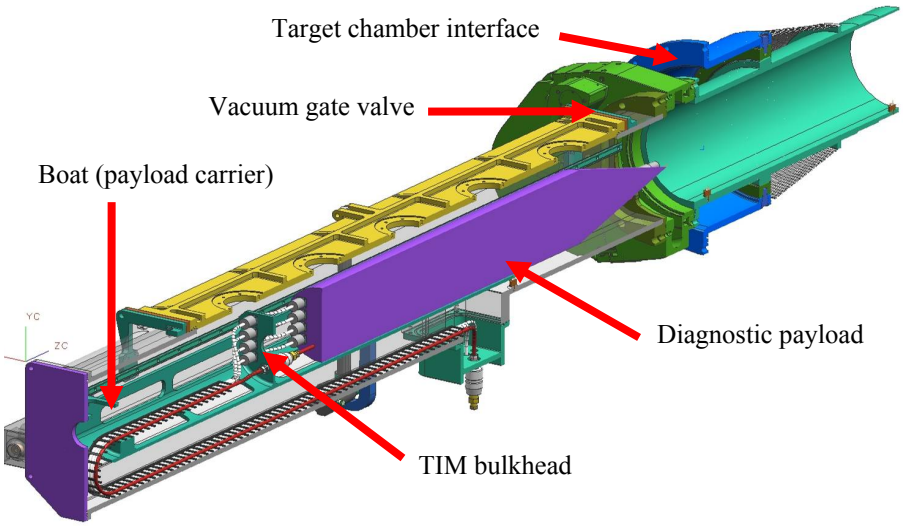

Figure 24: Cut-through drawing of a TIM attached to the target chamber showing an example diagnostic. [11]

HEX-ID will be placed in an equatorial target chamber TIM for ease of access and setting up, as heavy diagnostics require the use of cranes to load them into the TIM. Suitable TIM locations are port numbers 76 and 17. Port 17 is the default choice as it gives a line-of-sight with the short-pulse lasers incident on the target at different angles with respect to the target normal; in port 76 these are roughly the same. Port 17 has been identified in *Figure 25*.

Figure 25: TIM locations on the Orion target chamber. Port 17 is identified as preferential port for HEX-ID. [16]

2.6.3 Vacuum Compatibility of HEX-ID

HEX-ID will be in vacuum and therefore must be vacuum compatible. Vent holes are required to allow air to escape from within the spectrometer and all surfaces should have minimal out-gassing. It will also be necessary to keep the detectors light-tight, but it should still be possible to evacuate the spectrometer. These considerations have been implemented into the design.

2.6.4 Overall Mass of HEX-ID

The total mass of HEX-ID and the airbox currently stands at approximately 51 kg. There is a TIM payload boat weight limit on Orion of 60kg, whereas OMEGA has a weight limit of 45 kg. Work was carried out to reduce the overall mass of the diagnostic to meet the OMEGA requirements. This included reducing the thickness of Tungsten components within the spectrometer and reducing the length of the airbox to a minimum. These have made a significant reduction in the mass but compatibility with OMEGA TIMs still needs to be determined through consultation with LLE.

2.6.5 Thermal Loading of Airbox

The thermal loading was calculated for the airbox to establish the cooling requirements for the electronic components within the airbox. A water cooling system is available to each TIM but this would require additional engineering of the airbox design and increase the overall mass of the diagnostic. Assuming the airbox is entirely Aluminium, all heat is conducted to the airbox walls and all the power from cRIO is dissipated as heat (i.e. the cRIO is 0% efficient) then the time taken for the airbox to rise in temperature by 50 K is given by:

$$t = \frac{M_A c_{Al} \Delta T}{P_C}$$

Equation 5

where: M_A is the mass of the airbox (20 kg);
P_C is the maximum power output of the cRIO (17 W);
ΔT is the maximum temperature rise of cRIO (50 K); and
c_{Al} is the specific heat capacity of Aluminium (0.91 kJ/kg/K).

This results in a time of 15 hours, so the time taken for the temperature of the airbox to rise 1 K is approximately 18 minutes. It is expected that the cRIO system will only be switched on for about 30 minutes at a time so the cooling system, which generally takes the form of water cooling running through a copper plate, is not deemed necessary.

3.0 CHARACTERISATION EXPERIMENTS

In order that the diagnostic design could be corroborated and the HEX-ID built, characterisation of key components required to be carried out. This involved determining the best type of image plate for use in the finished spectrometer, measuring the x-ray reflectivity of the convex reflection crystals and determining the response of the CMOS sensors to x-rays.

3.1 Image Plate Resolution

At present, Fuji BAS TR image plate (IP) is used by the Plasma Physics Department (PPD) at AWE to obtain high resolution at low x-ray energies. Five different types of image plate from two manufacturers were sourced for a resolution comparison study and to justify the minimum spatial resolution assumed in resolving power calculations. The Manson x-ray facility at AWE was chosen to host these experiments due to the high source uniformity. A suitable energy was chosen from the range available and exposures of the IP carried out. A negative (clear pattern on a chrome background) resolution test target with the 1951 USAF resolution test pattern was obtained, which had a minimum element of group 3, element 6 (14.30 lp/mm or 35 μm). The pattern consists of groups of three horizontal and three vertical bars of varying dimensions. This was held in a mount in direct contact with a piece of IP. A table is included in *Appendix A.4* which details the resolution each element represents. Exposed IPs were scanned by one of two scanners (the Fuji FLA3000 and FLA7000) allowing spatial resolution comparison between different image plate systems to be carried out. The characteristics of each scanner are compared in *Table 5*. The FLA7000 is the scanner currently used with the Orion diagnostics. The resolution of the system is determined by clearly identifying the smallest element (two target elements of three line each, at right angles to each other).

IP scanner	FLA3000	FLA7000
Maximum laser power output (mW)	17	80
Laser wavelength (nm)	633	650
Laser spot diameter (μm)	190	244

Table 5: Characteristics of the Fuji FLA3000 and FLA7000 IP scanners [48].

3.1.1 Manson X-ray Facility Setup

The Manson x-ray facility at AWE is made up of the Model 5 multi-anode x-ray source, 20 kV power supply, x-ray source control instrumentation, vacuum pumps, and silicon drift detector. The Manson x-ray source is a thermionic diode with a pure Tungsten hairpin filament and a single electrostatic lens to focus the electron beam onto the target (anode) surface. The lens is made up of a high positive potential anode located within a coaxial-grounded cylindrical cavity. The lens images the tip of the filament onto the anode surface, and the spot where the electrons hit the surface is the source of x-rays. [49]

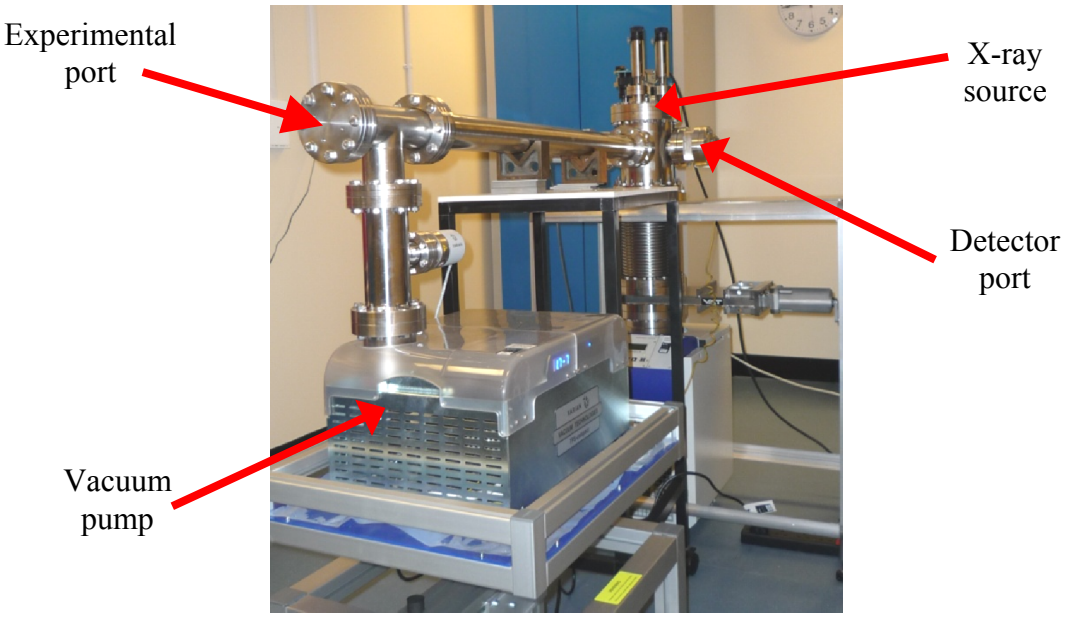

Figure 26: Photo of the Manson experimental set-up with the experimental port where the IP was held for exposures, pump to create a vacuum for free x-ray propagation and x-ray source chamber.

The two x-ray exit ports are shown in *Figure 26*. The experimental port was used to hold the IP and the unused detector port is at 90° to the first. Various anode materials can be selected by inserting the appropriate anodes and rotating a knob on the top of the x-ray source so that a selection of line energies can be produced. A list of the anodes available to the user is noted in *Table 6*. Different filters can be placed, again by the rotation of a knob, in the beam of x-rays as required to improve the spectral purity.

Target Material	Symbol	Line Energies (keV)
Copper	Cu-Lα	0.948
Aluminium	Al-Kα	1.487
Yttrium	Y-Lα	1.992
Zirconium	Zr-Lα	2.042
Molybdenum	Mo-Lα	2.29
Ruthenium	Ru-Lα	2.56
Silver	Ag-Lα	2.948
Tin	Sn-Lα	3.444
Titanium	Ti-Kα	4.51
Vanadium	V-Kα	4.952
Chromium	Cr-Kα	5.414
Manganese	Mn-Kα	5.898
Iron	Fe-Kα	6.403
Nickel	Ni-Kα	7.477
Zinc	Zn-Kα	8.638

Table 6: The x-ray line energies currently available from the Manson x-ray source.

A Vanadium anode with emission energy of 4952.2 eV was used with a selection of filter materials to give the best spectral purity at the Kα emission line. The Manson facility was operated at 10 keV and 5.5 mA heating current while the emission was recorded with a silicon drift detector using: no filter materials; 18 μm of Titanium; 6 μm of Vanadium; and 21 μm Titanium + 12.5 μm of Vanadium. Based on *Table 7* and *Figure 27*, the best filters to use were a combination of 21 μm Titanium and

12.5 µm of Vanadium, which significantly improved the spectral purity. Spectral purity, *SP*, was calculated using *Equation 6*:

$$SP = \frac{C_{peak}}{C_{total}} \times 100\%$$

Equation 6

where: C_{peak} is the number of counts within the peak; and

C_{total} is the total number of counts recorded.

The start of the peak was taken to be where the number of counts recorded reached approximately 300 and the end of the peak was where the number of counts recorded fell below this value again.

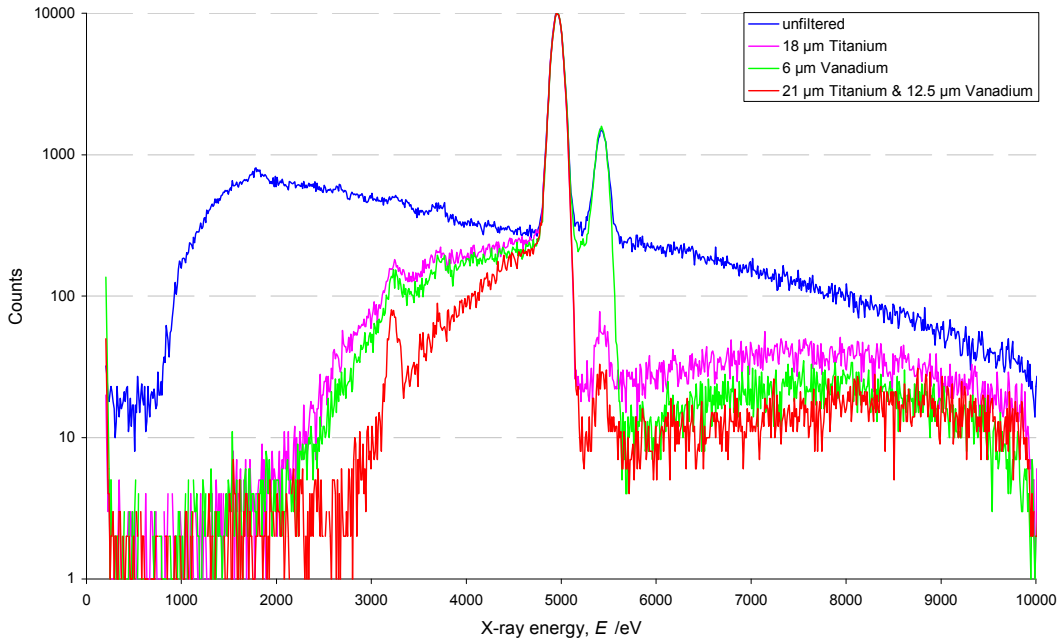

Figure 27: Spectrum recorded by the silicon drift detector with various filter materials in place to increase spectral purity for a Vanadium anode operated at 10 keV.

Filter selection	Spectral purity (%)
none	35.0
18 μm Titanium	72.7
6 μm of Vanadium	67.4
21 μm Titanium + 12.5 μm Vanadium	84.2

Table 7: Spectral purity values obtained from the x-ray spectrum recording of the Vanadium anode through various filters.

Small circles of each image plate type to be examined (Fuji TR, SR, MS and Kodak XL, HR) were cut to fit in the IP mounting device and erased before use by exposure to an intense halogen lighting screen. The resolution test target was placed over the IP and clamped in place. This was held in place on the end of the Manson experimental tube by a flange bolted in position. The system was evacuated of air to approximately $2x10^{-6}$ torr while the voltage was set to 10 kV and the current set to 1.5 mA. The gate valve was opened, power switched on to the anode and the timer started to expose the IP for the required time. Upon reaching this time the x-ray production was stopped, the gate valve was closed and the system brought back to atmospheric pressure. The IP was removed from its holder and kept sealed from light as it was transported to the IP scanner. Scanning took place quickly after exposure to avoid effects of fade, which can have a detrimental effect on resolution. The time between exposure and scanning was approximately five minutes for the FLA3000 exposures and approximately twenty minutes for the FLA7000 exposures due to the scanner being housed in another building. The IP scanner parameters detailed in *Table 8* are used in *Equation* 7 to calculate photo-stimulated luminescence (PSL) values from the greyscale values, *G*[16]:

$$PSL = \left(\frac{R}{100}\right)^2 \left(\frac{4000}{S}\right) 10^{L\left(\frac{G}{65536} - 0.5\right)}$$

Equation 7

Scanner	Sensitivity, *S*	Latitude, *L*	Scan resolution, *R* (μm)
Fuji FLA3000	4000	5	50
Fuji FLA7000	4000	5	25

Table 8: The parameters each scanner was set to before scanning each image plate.

Analysis of the scanned image was carried out to determine if the time of exposure needed to be modified to avoid saturation or maximise signal level. The best exposure time was used to obtain three repeat exposures under the same conditions on the same day. These are then analysed to determine the spatial resolution of each IP type.

3.1.2 Resolution Test Results

Figure 28 shows two examples of exposed Fuji BAS TR IP scanned on the FLA3000 and FLA7000 scanners respectively. It is very clear that the quality of the image from the FLA7000 is much better due to its smaller scan resolution of 25 μm compared to the 50 μm of the FLA3000.

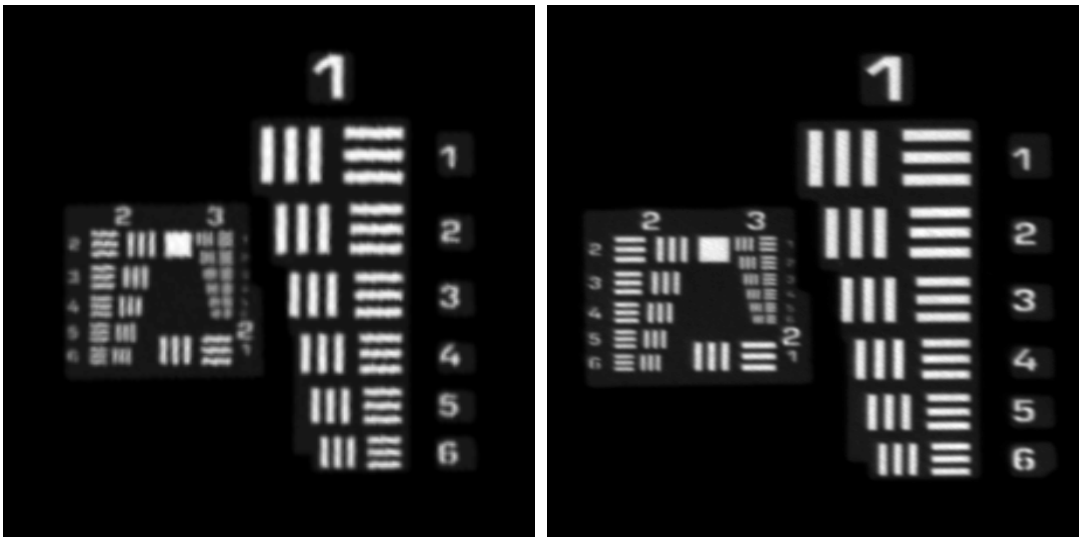

Figure 28: Resolution test target images for Fuji BAS TR image plate scanned on the FLA3000 (left) and FLA7000 (right) scanners.

Determining the smallest element visible to the human eye is purely subjective so to quantify the spatial resolution of the image plate types, the contrast transfer function (CTF) was calculated [14, 26]:

$$CTF = \frac{I_{\max} - I_{\min}}{I_{\max} + I_{\min}}$$

Equation 8

where I_{max} and I_{min} are the maximum and minimum intensities of each element taken by a lineout process through the final processed image. *Figure 29* shows the plot of the calculated CTF against resolution in lp/mm while *Table 9* gives the maximum achievable resolution for each type of IP scanned using the Fuji FLA3000. This was taken to be the last data point before the CTF reduced to zero.

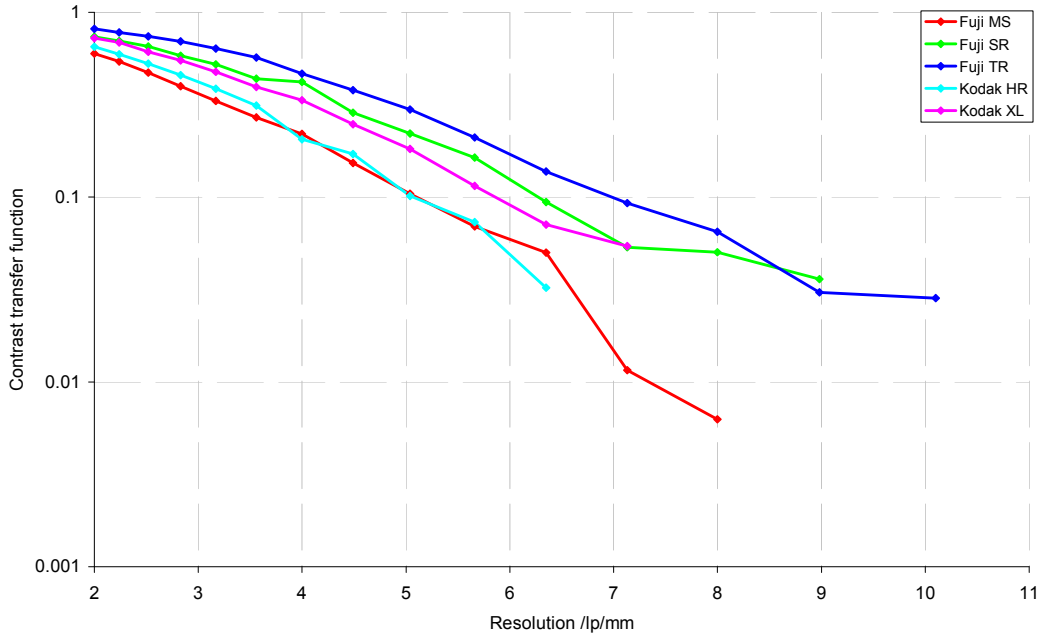

Figure 29: Contrast transfer function (CTF) plotted against resolution in line pairs per millimetre for the Fuji FLA3000 scanner.

IP type	Time (mins)	Smallest element (group, element)	Resolution (lp/mm)	Resolution (μm)
Fuji MS	5	3,1	8	62.5
Fuji SR	8	3,2	8.98	55.7
Fuji TR	6.5	3,3	10.1	49.5
Kodak HR	4	2,5	6.35	78.7
Kodak XL	5	2,6	7.13	70.1

Table 9: Maximum resolution achievable from each IP exposed at 4.95 keV on the Manson facility and scanned with the Fuji FLA3000.

The resolution limit was not determined by the image plate, but rather by the intrinsic limit of the FLA3000 scanner as the grain size of the IP is much smaller. Additional scans were carried out using the FLA7000 scanner, which has a smaller scan resolution. Due to the different resolution setting used for the FLA3000 and FLA7000 scanners, the saturation levels were different (*Equation 7*) and the times for exposures had to be changed. Analysis of the data was carried out again and the CTF calculated (*Figure 30* and *Table 10*).

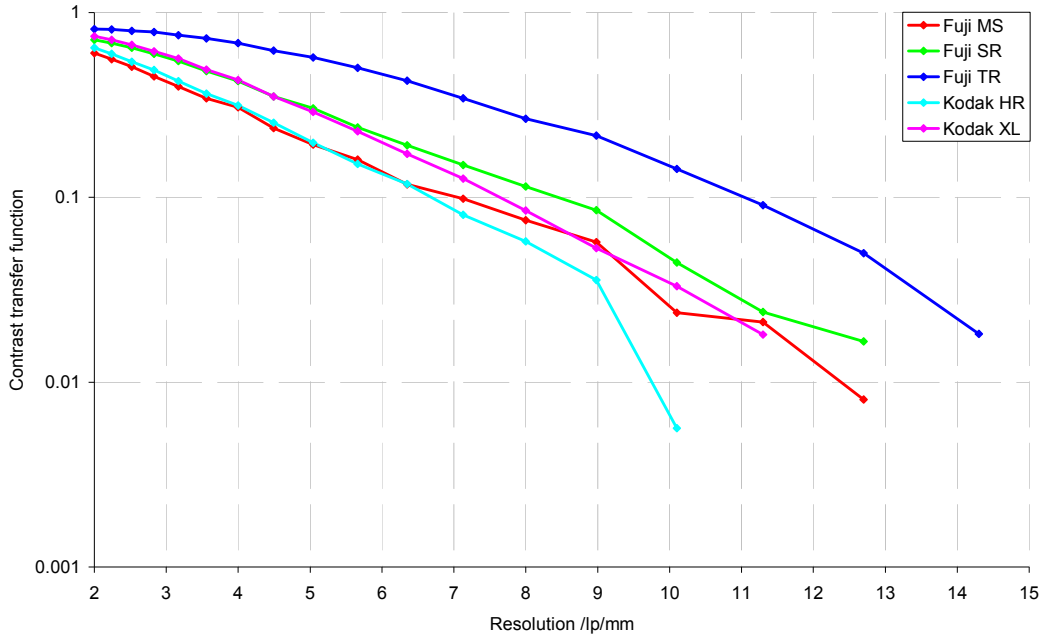

Figure 30: Contrast transfer function (CTF) plotted against resolution in line pairs per millimetre for the FLA7000 scanner.

IP type	Time (mins)	Smallest element (group, element)	Resolution (lp/mm)	Resolution (μm)
Fuji MS	3	3,5	12.7	39.4
Fuji SR	5.5	3,5	12.7	39.4
Fuji TR	4.5	3,6	14.3	35
Kodak HR	3.5	3,3	10.1	49.5
Kodak XL	3	3,4	11.3	44.2

Table 10: Maximum resolution achievable from each IP exposed at 4.95 keV on the Manson facility and scanned with the Fuji FLA7000.

On comparison between *Table 9* and *Table 10,* it is clear that the Fuji TR IP has the highest resolution at 4.95 keV and the use of the FLA7000 scanner has improved the maximum achievable resolution for all types of IP. *Figure 31* and *Figure 32* show the direct comparison of the FLA3000 and FLA7000 data for all image plates tested.

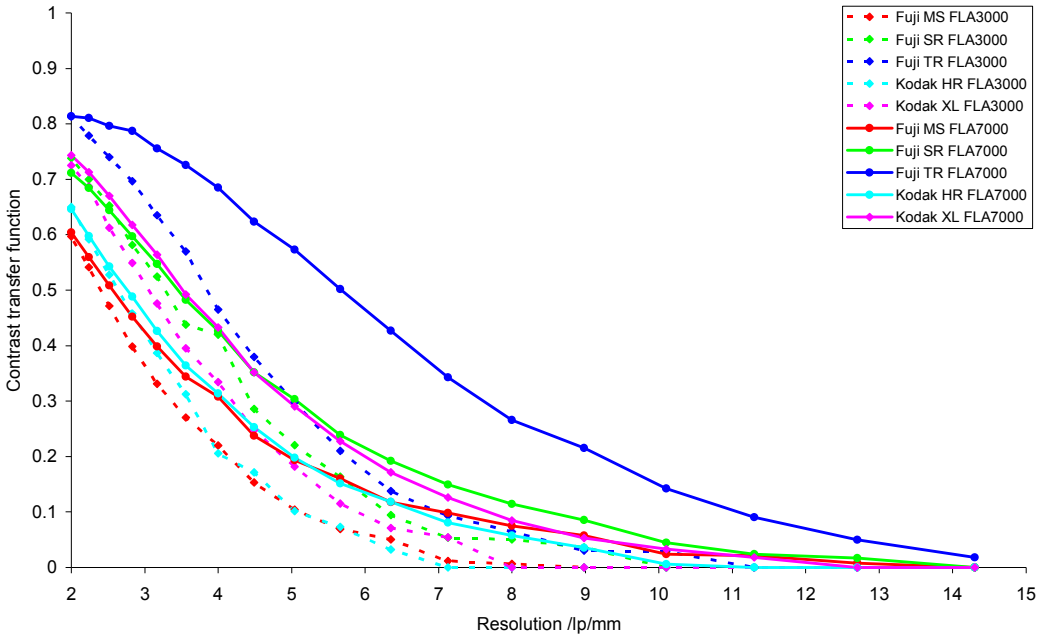

Figure 31: Contrast transfer function (CTF) direct comparison between the Fuji FLA3000 (dotted) and FLA7000 (solid) scanners for each type of IP.

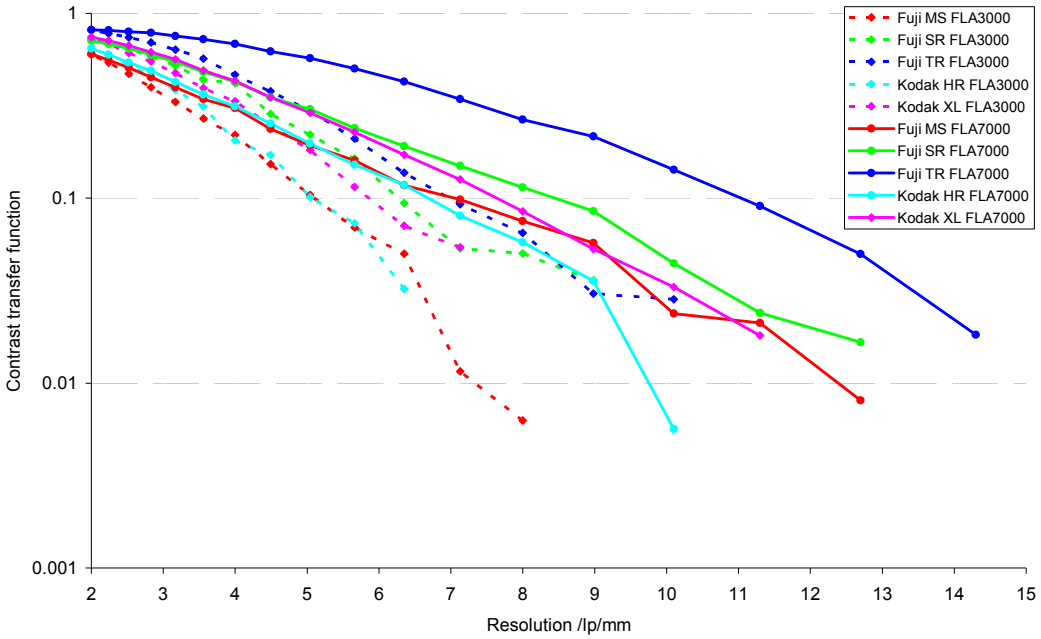

Figure 32: Contrast transfer function (CTF) direct comparison between the Fuji FLA3000 (dotted) and FLA7000 (solid) scanners for each type of IP showing the limit of resolution.

A resolution comparison of each type of IP tested on both the Fuji FLA3000 and FLA7000 scanners at a constant CTF value of 0.06 is shown in *Table 11*. This shows the same trend as *Table 9* and *Table 10* in that the Fuji TR image plate has the highest CTF and smallest resolution. As a result of this, it will be used with the HEX-ID spectrometer when it is in operation and scanned using the Fuji FLA7000 scanner.

Scanner	IP type	Resolution (lp/mm)	Resolution (μm)
FLA3000	Fuji MS	6	83.3
	Fuji SR	6.95	71.9
	Fuji TR	8.1	61.7
	Kodak HR	5.8	86.2
	Kodak XL	6.8	73.5
FLA7000	Fuji MS	8.8	56.8
	Fuji SR	9.6	52.1
	Fuji TR	12.5	40.0
	Kodak HR	7.9	63.3
	Kodak XL	8.7	57.5

Table 11: Comparison of the achievable resolution of each type of image plate tested on both scanners at a constant CTF value of 0.06.

3.2 Crystal Reflectivity

The peak locations and integrated reflectivity of x-rays from the convex crystals, attached to their mounts, were measured at several energies in the range 1 to 10 keV. Eight crystals were purchased in total (four for each of the two spectrometers), although only one set required full characterisation, while the remaining set would have a limited set of measurements taken for comparison.

3.2.1 Excalibur X-ray Source Setup

The Excalibur facility at AWE is capable of producing soft x-rays in the range of approximately 0.5 to 8 keV. It is constructed of a vacuum chamber with a dc x-ray tube mounted on the side and the associated vacuum pumps, power supply and electronic instruments. A multifaceted target block is the anode and each facet is coated in a different material. The target block is rotated prior to use to select the desire target material. Applying a large current to the filament array (cathode) in front of the target spot, and applying a suitable large voltage causes the production of x-rays. A proportional counter is used as the detector of x-rays. [27, 50]

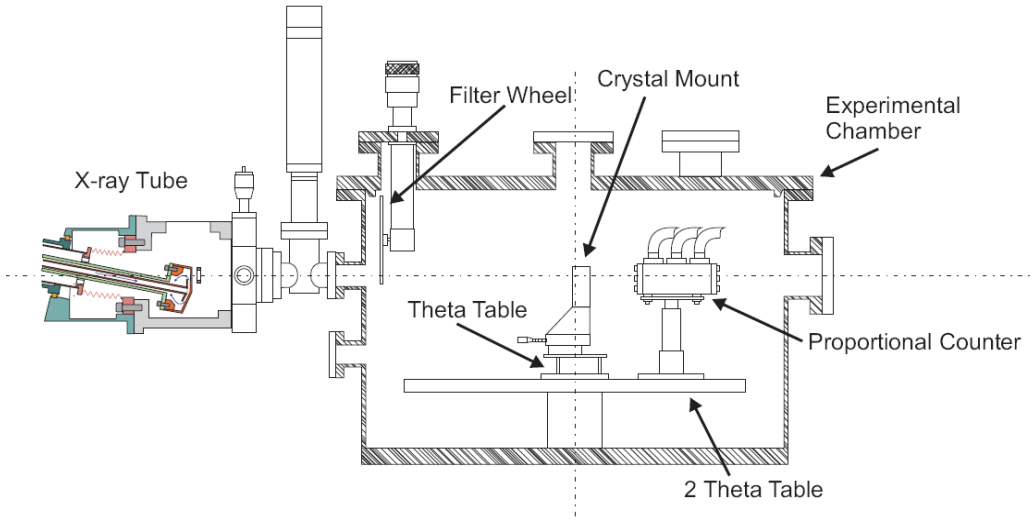

Figure 33: Schematic diagram of the Excalibur x-ray source and vacuum experimental chamber. [51]

Excalibur has two rotating tables inside the vacuum chamber – one is used to hold the crystal and the other is used to hold the detector (*Figure 33*). The crystal was installed on a kinematic mount on the θ table in the centre of the chamber. The proportional counter (P-C) was mounted on the 2θ table away from the centre. A diagram of the setup is shown in *Figure 34* and the table rotation is controlled via a LabView program. The crystal mount was levelled horizontally and the height of the P-C was adjusted to align with the centre of the crystal. The base of the crystal mount was aligned parallel with the beam. The crystal was positioned so that the beam hit close to the centre of the crystal. The beam slit width was set to 10 mm to expose a large area of the crystal to the x-rays.

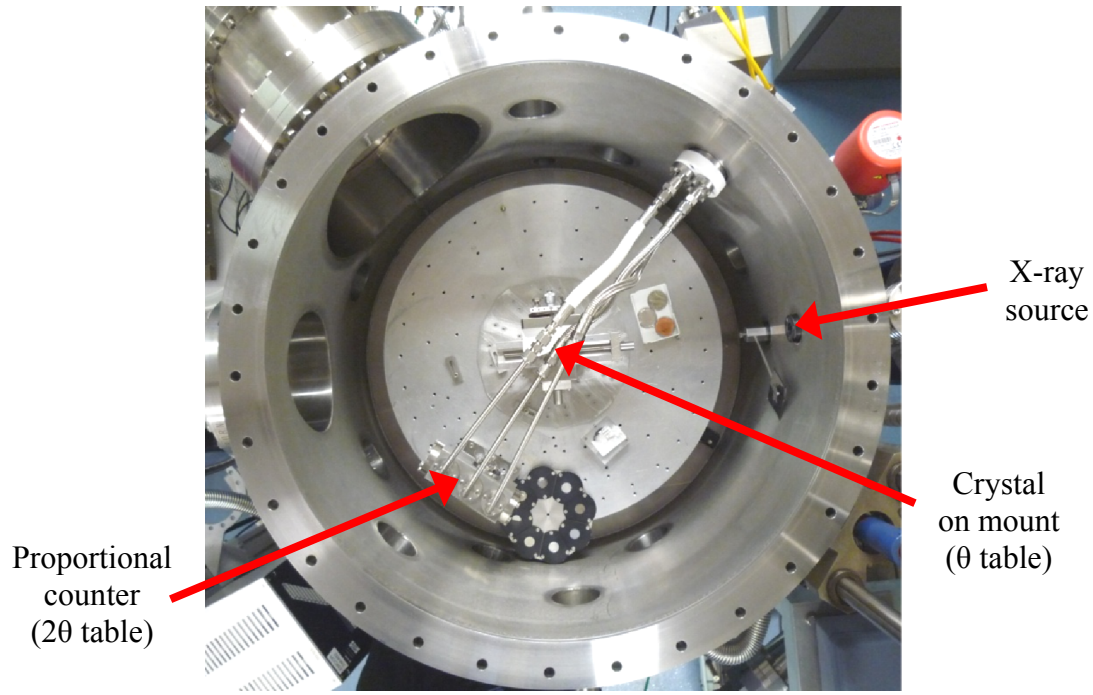

Figure 34: Picture from above of experimental set up within Excalibur chamber showing the proportional counter and hoses, crystal on a kinematic mount in the centre and the source of x-rays.

The available target energies are noted in *Table 12*, which were plotted with the Bragg angle against energy. The limit of rotation for the 2θ table is 80° so the Bragg angle limit to measure the reflectivity was 40°. From this, six characteristic lines energies were chosen (*Figure 35*). Three energies for each crystal would cover the range of energies they are to be used within the finished diagnostic, and Manganese-Kα was chosen as a common energy for all crystals. Crystals from set number one were examined first at a range of energies, while crystals from set number two were only to be examined at Mn-Kα energy. If the reflectivity values were similar then no further testing would be carried out.

Target Number	Target Material	Symbol	Kα Line Energies (keV)	Lα Line Energies (keV)
1	Titanium	Ti	4.51	0.452
2	Zirconium	Zr	-	2.042
3	Manganese	Mn	5.898	0.636
4	Cobalt	Co	6.93	0.775
5	Copper	Cu	8.047	0.928
6	Ruthenium	Ru	-	2.558
7	Antimony	Sb	-	3.605
8	Chromium	Cr	5.414	0.571
9	Silver	Ag	-	2.984
10	Aluminium	Al	1.487	-

Table 12: The x-ray line energies that the Excalibur facility can produce upon selection of the appropriate target.

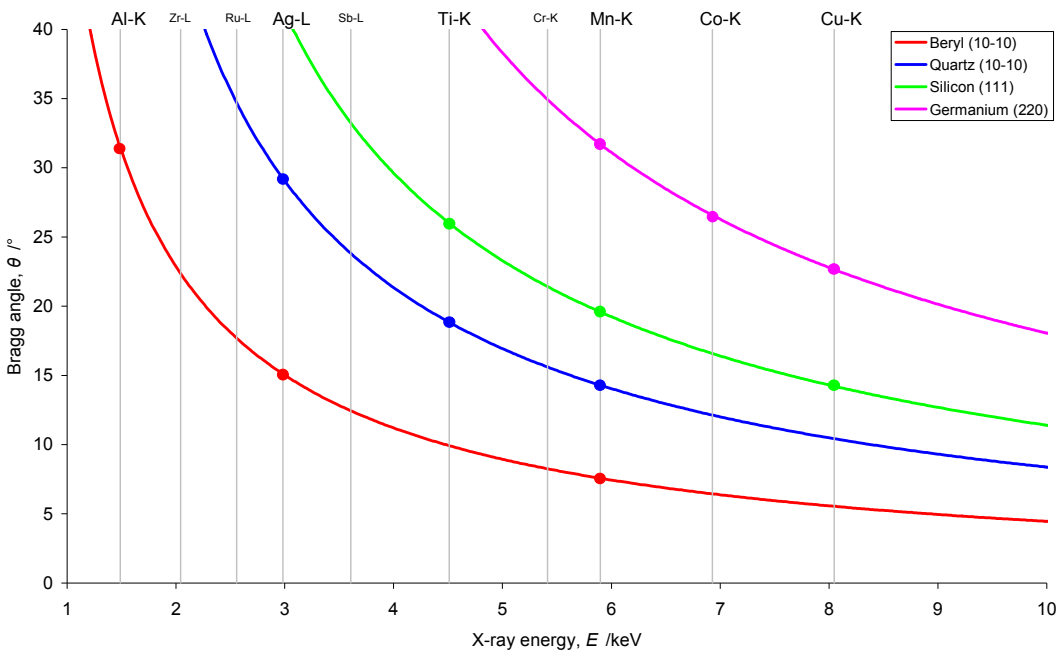

Figure 35: Bragg angle varying with energy for each of the four crystals. The x-ray energies available from Excalibur (vertical lines) and those used (dots) are marked.

The settings used on Excalibur for each of the targets used are noted in *Table 13*. The target voltage was accurately held constant between different experiments. The current indicator gauge was not as accurate as the voltage gauge, but every effort was made to keep the current constant between experiments.

Crystal	Line Energies (keV)	Target	Voltage (kV)	Current (mA)
Beryl	1.487	Al-Kα	3	80
	2.984	Ag-Lα	7.5	150
	5.898	Mn-Kα	12	100
Quartz	2.984	Ag-Lα	7.5	150
	4.51	Ti-Kα	9	110
	5.898	Mn-Kα	12	100
Silicon	4.51	Ti-Kα	9	110
	5.898	Mn-Kα	12	100
	8.047	Cu-Kα	16	35
Germanium	5.898	Mn-Kα	12	100
	6.93	Co-Kα	14	30
	8.047	Cu-Kα	16	35

Table 13: Excalibur target parameters used for each crystal examined.

The proportional counter and amplifier were set up with the following parameters: voltage of 1400 V; gas pressure of 700 Torr; course gain of 100; fine gain of 10.0; and shape of 1 μs. The discriminator of the multi-channel analyser was set to 165 removing any noise contribution. For the Al-Kα target only, the course gain was set to 300 and voltage of 1370 V.

3.2.2 Peak Reflectivity Locations

Three scans were carried out to accurately determine the x-ray flux reflected off the crystal as outlined in *Table 14*. The rough scan (*Figure 36*) was used to quickly find any peaks detected from the crystal. A rocking curve scan (*Figure 37*) was carried out to determine if slight alterations to the crystal position affected the signal at the peak. Then, a slow fine scan (*Figure 38*) was carried out over the peak position using the ideal θ value obtained from the rocking curve scan. The peaks are quite broad due to the slit width being 10 mm. This was noted in previous work looking at the x-ray beam profile variations with width [52]. From all these results, the position of the peak reflectivity off each crystal was recorded in *Table 15*.

Stage		θ start (°)	Increment (°)	Sets	θ end (°)	Count time (s)
1 – Rough scans	θ	0	-	-	-	3
	2θ	0	0.3	100	29.7	
		25			54.7	
		50			79.7	
2 – Rocking curve	θ	-0.27	0.06	10	0.27	3
	2θ	*x*	0.05	61	*x* + (61*0.05)	
3 – Fine scan	θ	θ_{peak}	-	-	-	100
	2θ	*x*	0.05	71	*x* + (71*0.05)	

Table 14: The three stages of scans required to pinpoint the peak reflectivity of each crystal and x-ray energy. x is a suitable position just before the peak determined by the rough scans and θ_{peak} is the optimum value obtained from the rocking curve scan.

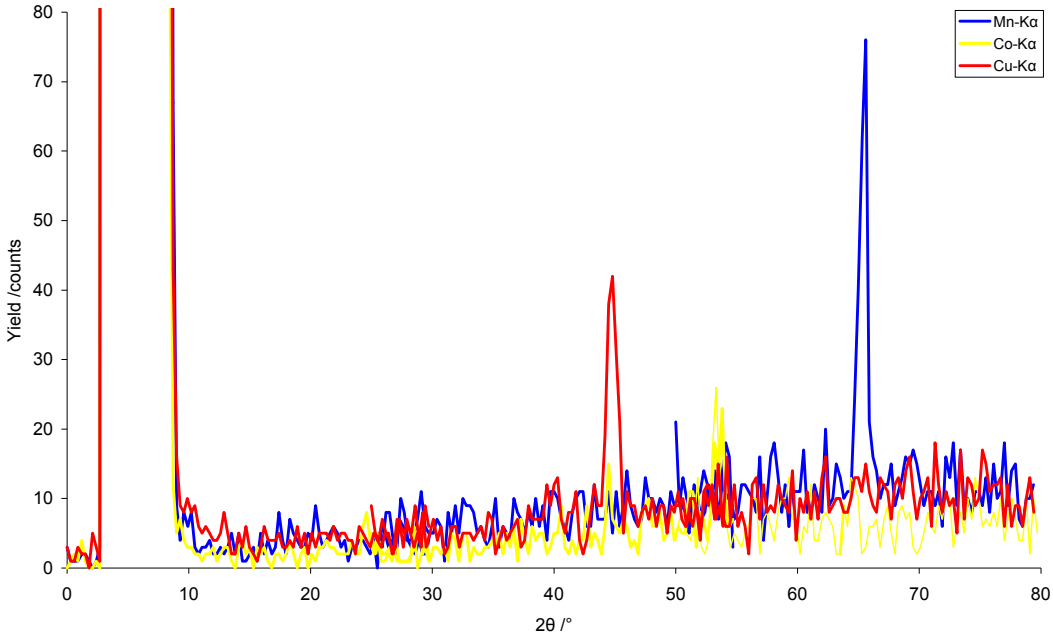

Figure 36: Rough scans combined into single figure for Germanium crystal exposed to Mn-Kα, Co-Kα and Cu-Kα x-rays.

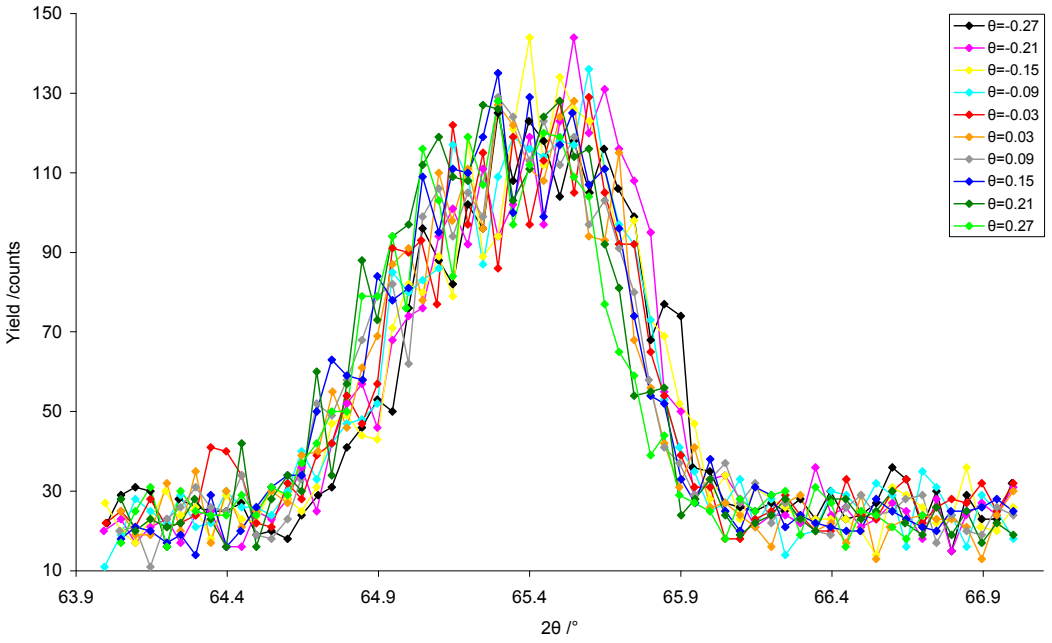

Figure 37: Rocking curve data for Germanium crystal exposed to Mn-Kα x-rays of energy 5.898 keV.

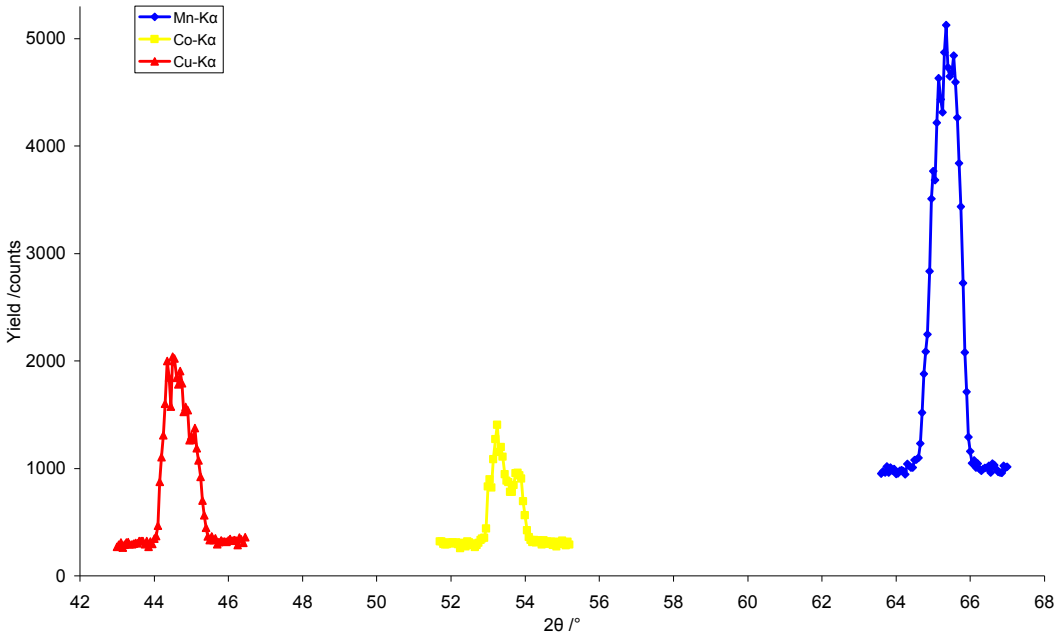

Figure 38: Fine scan data for Germanium crystal exposed to Mn-Kα, Co-Kα and Cu-Kα x-rays.

Crystal	Target	Energy	θ peak (°)	2θ peak (°)
Beryl	Al-Kα	1.487	-	-
	Ag-Lα	2.984	-	-
	Mn-Kα	5.898	-	-
Quartz	Ag-Lα	2.984	-0.03	58.746
	Ti-Kα	4.51	-0.21	36.8
	Mn-Kα	5.898	-0.15	27.798
Silicon	Ti-Kα	4.51	-0.09	52.248
	Mn-Kα	5.898	-0.15	38.502
	Cu-Kα	8.047	-0.09	27.498
Germanium	Mn-Kα	5.898	-0.15	65.348
	Co-Kα	6.93	-0.15	53.246
	Cu-Kα	8.047	-0.09	44.5

Table 15: θ and 2θ positions of peak reflections from each of the four crystals examined.

Peak positions for the Beryl crystal could not be determined due to the appearance of two peaks in the recorded data at the same location despite changing the x-ray energy. These peaks can be seen in *Figure 39* for Al-Kα, Ag-Lα and Mn-Kα energies. It is thought that the two peaks relate to fluorescence from Silicon and Aluminium present within the Beryl crystal. Time constraints prevented further investigation of the Beryl crystal but a potential solution of using flat crystal geometry rather than a bent one was looked at. The spectral range was calculated for a number of crystal materials in an effort to fill the Channel 1 gap but this range was not sufficient based on existing dimensions of the spectrometer. This is an area that still requires a great deal of further work, although the x-ray transmission values for the crystals in the range of 1 to 10 keV were calculated using The Center for X-ray Optics database [53] and shown in *Figure 40*. This provides an indication that the thinner Beryl crystal was not ideal due to the high transmission values.

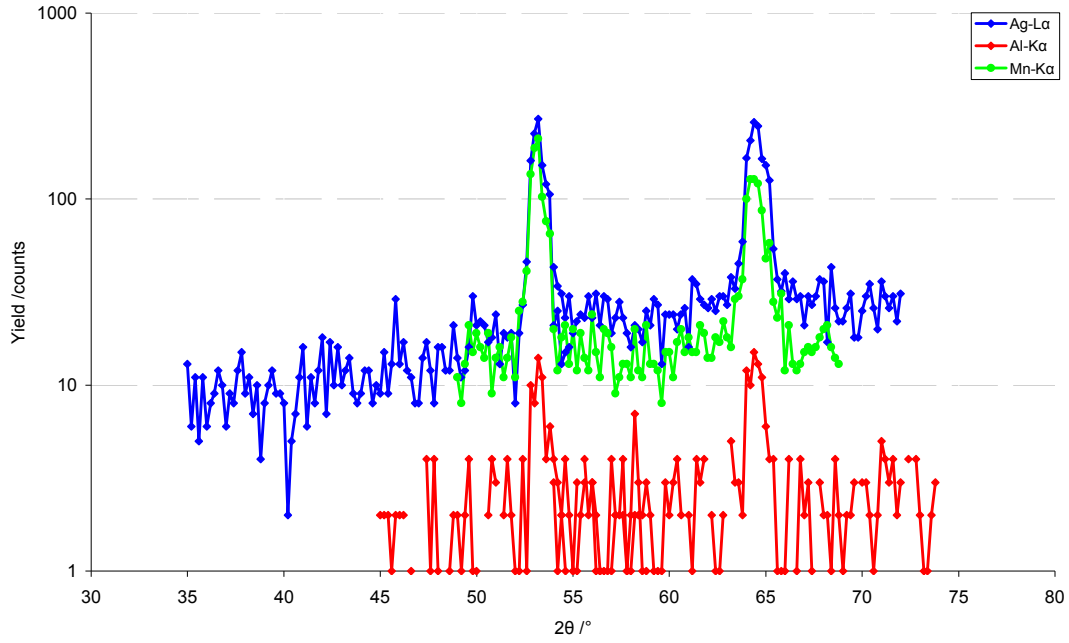

Figure 39: Rough scans on the Beryl crystal showing fluorescence peaks at 2θ values of 53° and 64° only.

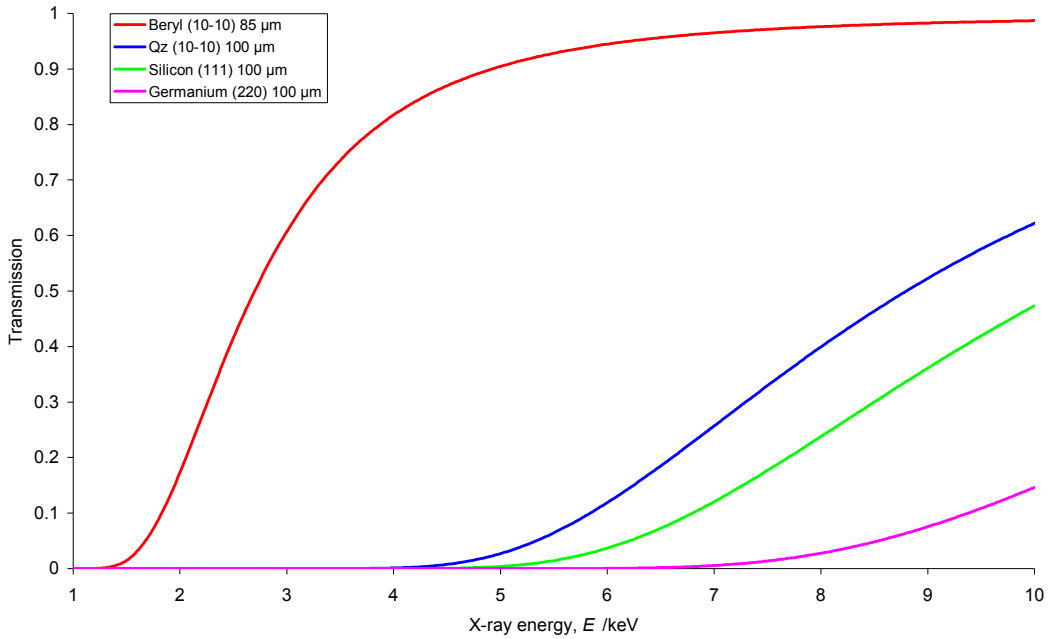

Figure 40: Transmission of x-rays through the final selection of crystals over the range of 1 to 10 keV.

3.2.3 Integrated Reflectivity Measurements

A ten minute long recording of the signal was taken using the MCA (*Figure 41*) with the proportional counter set at the peak intensity position noted in *Table 15*. This was compared to the direct signal strength from the source measured through a filter material (*Table 16*), but without the crystal or mount in place.

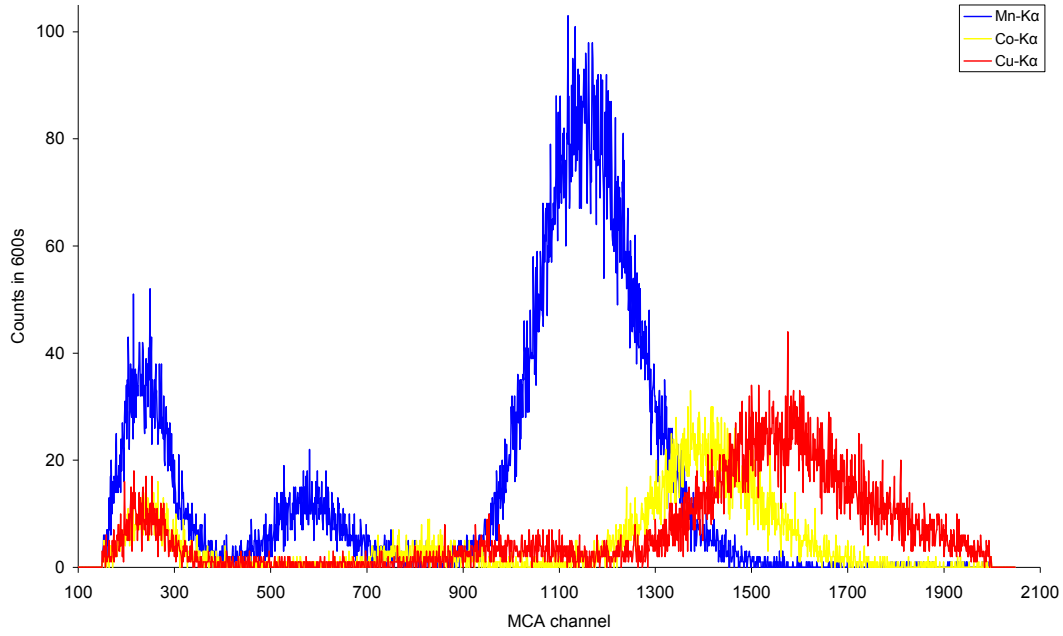

Figure 41: Multichannel analyser (MCA) counts measured over a ten minute period with peak reflection from the Germanium crystal.

Filter number	Material	Thickness (μm)	Target
1	Fe	20	Co-Kα
2	-	-	-
3	Ni	25	Cu-Kα
4	Ag	5	Ag-Lα
5	Al	6	Al-Kα
6	Ti	25	Ti-Kα
7	Cr + epoxy resin	25 + 1085	Mn-Kα
8	In	10	Sb-Lα

Table 16: The filter materials used for each of the source measurements.

The measurement of the source was taken after experiments with the Silicon crystal had been carried out. Ideally the source measurements would have been taken directly before and after the reflectivity measurements of each crystal and at each energy used. This was not practical due to vacuum equipment problems and the length of time required to open the system, remove the crystal and mount, and pump down to vacuum.

The peak of the source was found using the rough scan parameters detailed in *Table 17* and the results of which are shown in *Figure 42*. The P-C was positioned on this peak and used to record 500000 counts on the MCA (*Figure 43*). This arbitrary value was chosen as it was sufficient to record the source strength but took a short enough time that repeat measurements could be taken. This was done for each of the x-ray energies required to examine the four crystals. The Al-Kα peak is offset to higher MCA channels due to the slight alterations in the settings of the P-C and amplifier.

Stage		θ start (°)	Increment (°)	Sets	θ end (°)	Count time (s)
Rough scan	θ	0	-	-	-	1
	2θ	-10	0.2	100	9.8	

Table 17: Rough scan used to find peak of source with no crystal.

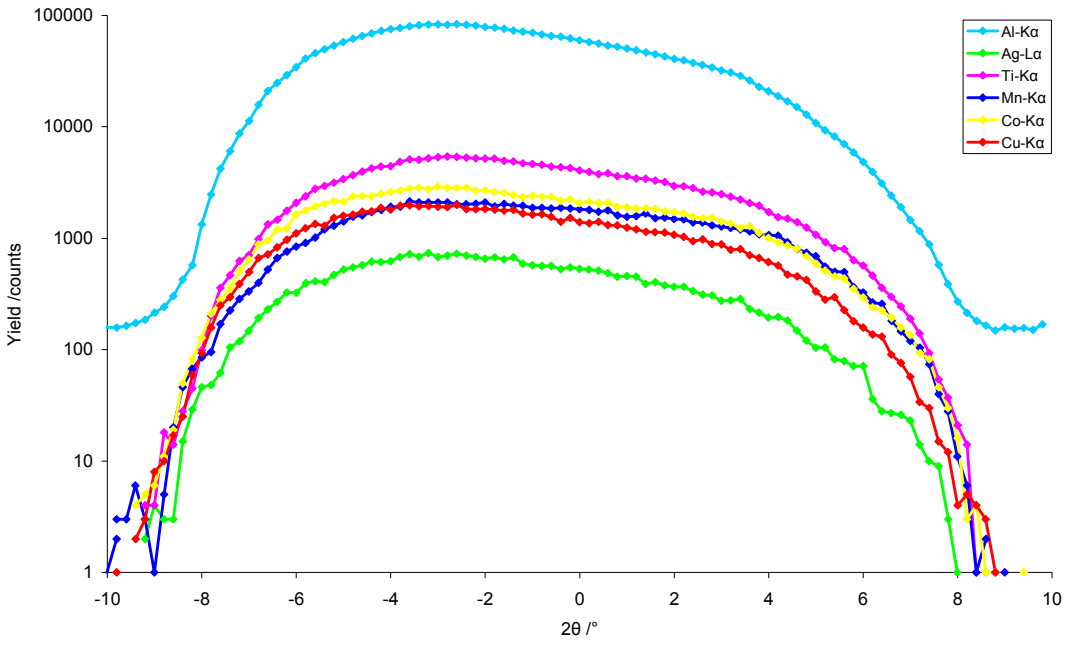

Figure 42: The 2θ position of the peak x-ray flux from Excalibur through filter materials but with no crystal present.

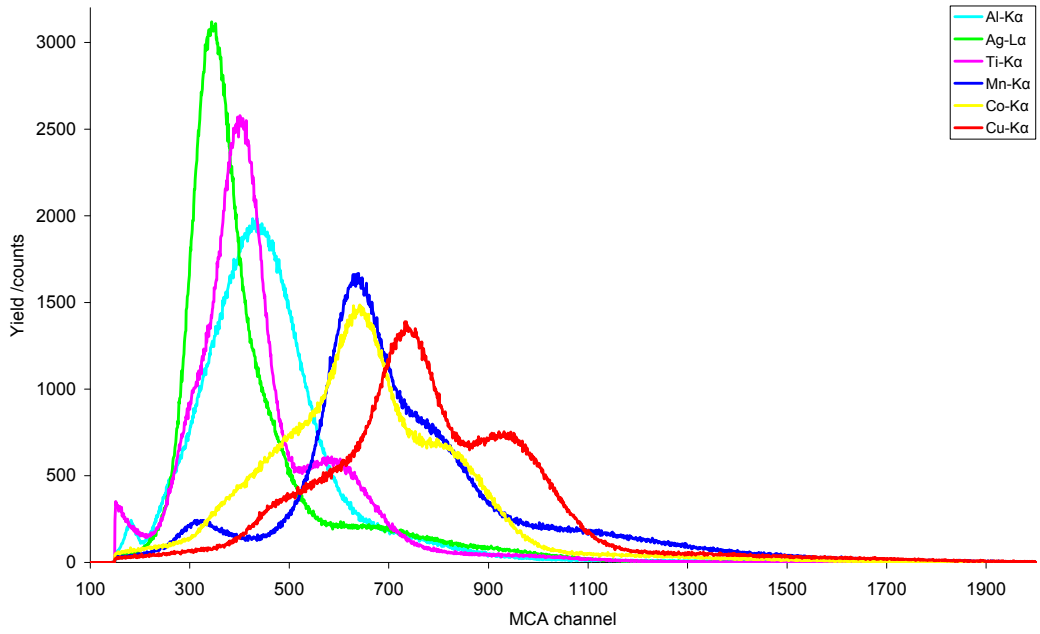

Figure 43: Integrated value of 500000 counts recorded from each target energy used during the reflectivity measurements.

The integrated reflectivity was calculated using *Equation 9* where the integrated number of counts was calculated for each peak measurement and the live time was the time the proportional counter measured the x-rays. The filter transmission was calculated based on the thickness and the mass absorption coefficient for each of the filter materials. The final calculated values for the integrated reflectivity of the three crystals examined are shown in *Figure 44*.

$$IR = \frac{CR_{crystal}}{CR_{source}} \times 100\%$$

Equation 9

where: IR is the integrated reflectivity (%);

$$CR_{crystal} = \frac{C}{t};$$

$$CR_{source} = \frac{C/FT}{t};$$

C is the integrated number of counts;

t is the live time (s); and

FT is the filter transmission value.

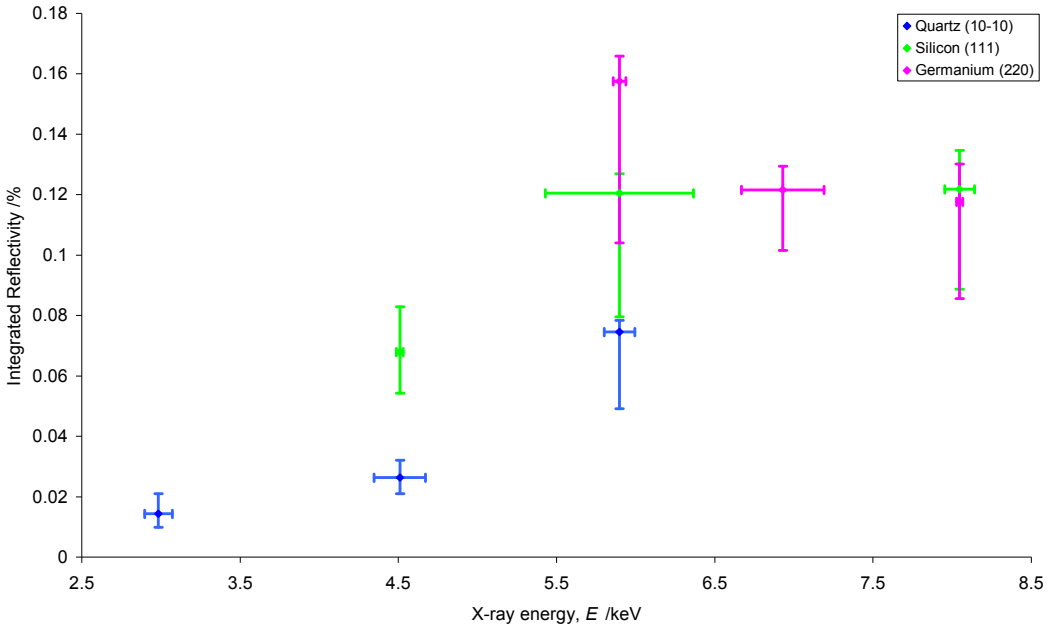

Figure 44: The results of the integrated reflectivity calculations for each of the crystals examined – Quartz (10-10), Silicon (111) and Germanium (220).

The Mn-Kα common energy displayed in *Figure 44* shows that the order of decreasing crystal reflectivity is Germanium then Silicon then Quartz. This was the expected order based on information provided by the manufacturer. There would appear to be a general trend of increasing reflectivity when higher energy x-rays are incident on the crystal surface.

The filter material used during the Mn-Kα source measurements was 25 μm Cr with an epoxy resin backing. The thickness and composition of the epoxy resin was not specified. The total filter thickness was measured to be 1.11 mm and samples were sent for EDS (energy dispersive x-ray analysis) elemental analysis. The main constituent elements that were present are Carbon (59.3%), Nitrogen (15.7%), Oxygen (24.9%) and Aluminium (0.34%). Hydrogen was also expected but the technique used could not detect it. From this the x-ray transmission was calculated although could not be confirmed to be absolutely accurate.

From operator knowledge, an energy error is 5% is expected [52]. The x-axis errors shown are calculated from calibration of the MCA channel that each peak was seen compared to the true energy for each characteristic x-ray energy. This only examined the P-C detector error and if time had permitted then additional work would have been carried out to determine the spectral purity of the source using a calibrated silicon drift detector. Y-axis errors were determined from the width of a Gaussian peak fitted to the P-C ten minute peak count at the position of peak reflectivity. This was factored into the filter transmission for the source measurements to determine the range of integrated reflectivity values possible for each energy and crystal.

3.3 CMOS Response

In order to characterise the CMOS sensors a wiring system was constructed as shown in *Figure 45* with the cRIO, power supplies, CMOS sensor and associated wiring.

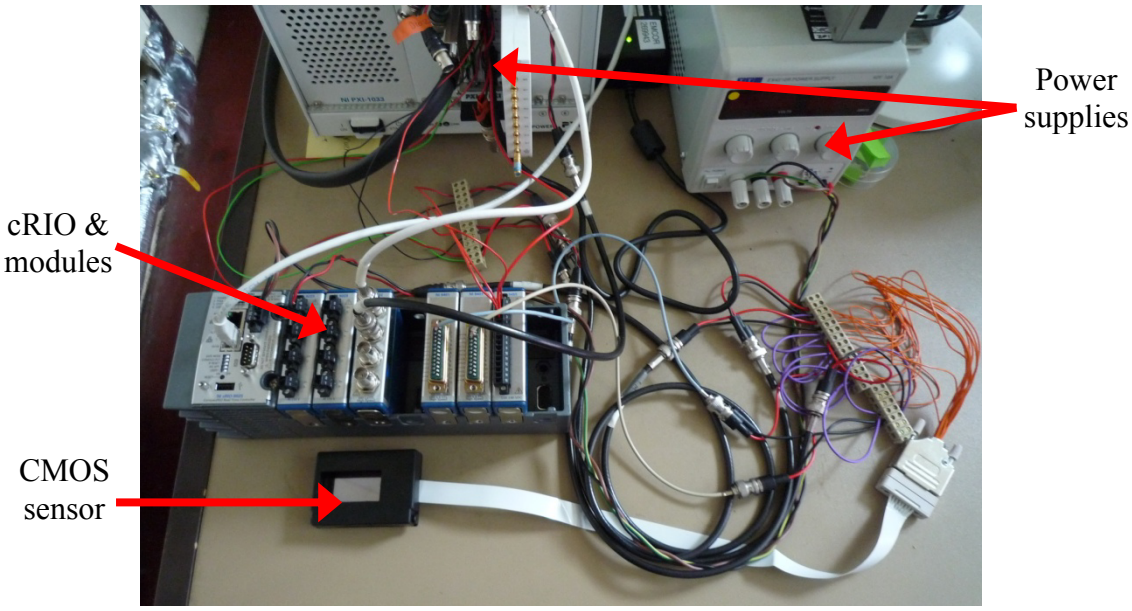

Figure 45: The electronic setup to control the CMOS sensor and retrieve optical images for download onto a computer.

3.3.1 Resolution Tests

Similar to the IP resolution tests carried out previously, the CMOS sensor was also tested to determine its resolution limit. This was done with visible light rather than the x-rays used to expose the IP because the sensors are inherently sensitive to visible light, and the addition of a scintillator to detect x-rays would have had a detrimental effect on resolution. The resolution test target was placed directly onto the sensor surface and a LED used to illuminate both from above. *Equation 8* was used as before to calculate the Contrast Transfer Function (CTF) of the resolution test target elements in the processed image. *Figure 47* shows the varying spread in CTF values obtained from the CMOS images. This was due to the test target not being compressed against the surface of the sensor as it was with the IP, allowing light to enter from numerous directions.

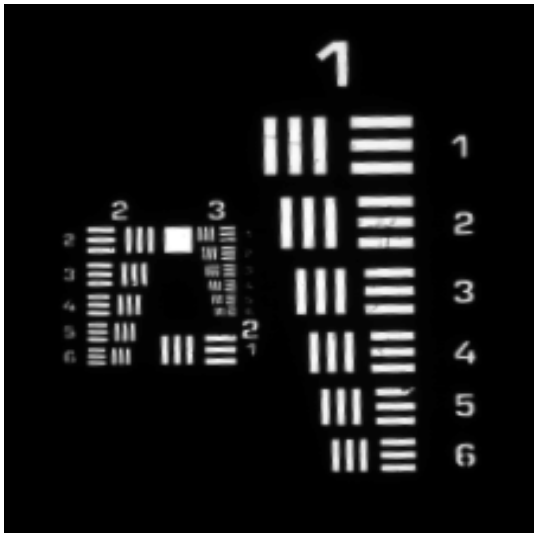

Figure 46: Resolution test target image using CMOS sensor as detector.

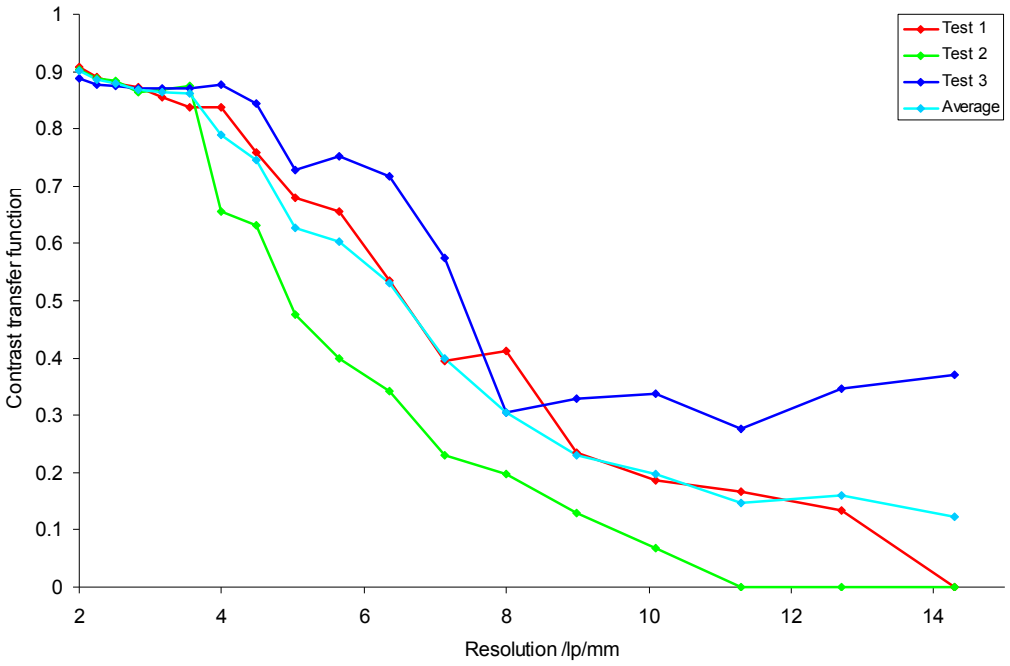

Figure 47: Contrast transfer function (CTF) plotted against resolution in line pairs per millimetre for the CMOS sensor repeated three times and average values calculated.

Upon comparison with the IP resolution tests it can be seen that for visible light the CMOS sensor can achieve the same resolution of 35.0 µm as the Fuji BAS TR image plate. There is a significant improvement in the CTF at this resolution as well. IP is becoming more expensive to purchase and will be gradually phased out, so using electronic sensors that can achieve the same or better resolution is very desirable. From this work it would appear that the Radeye 1 CMOS sensors can meet the requirements of providing resolving power and allowing remote imaging.

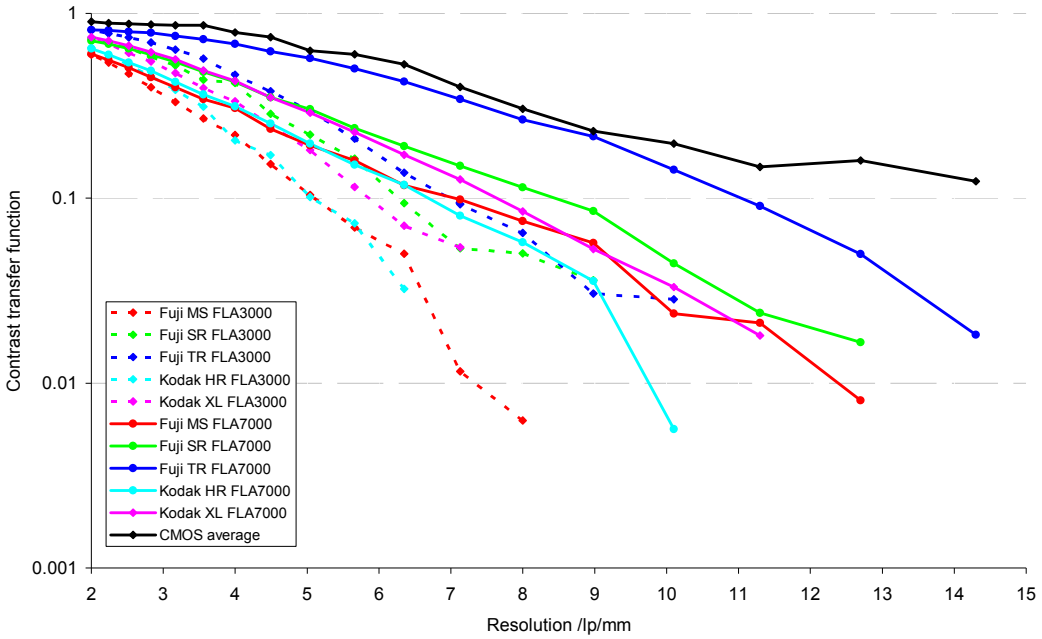

Figure 48: Comparison of CMOS sensor resolution limit to the image plate tests carried out previously.

3.3.2 X-ray Detection

The CMOS sensors detect visible light by default, but will require a scintillator material to convert x-rays into visible photons for detection [24]. Options for scintillator materials are being considered from Applied Scintillation Technologies, Ltd. This company will be able to provide a coating on the CMOS to convert the x-rays in the range of 1 to 10 keV into visible light. Gadolinium Oxysulphide doped with Terbium (Gd_2O_2S:Tb) is very efficient in converting incident x-rays into visible light. It is effective at stopping x-rays due to its high atomic number and density. Rapid scattering of the light is a major factor for Gd_2O_2S:Tb though with very thin screens required for high resolution imaging. [54]

Table 18 provides some specifications for comparison of scintillator materials available. Columnar-grown Cesium Iodide (CsI:Tl) has a higher maximum achievable resolutions of >18 lp/mm compared to 12-14 lp/mm achievable from Gd_2O_2S:Tb. CsI:Tl has higher efficiency for soft x-rays whereas Gd_2O_2S:Tb has superior efficiency for higher energies. From this it would seem clear that CsI:Tl is

the preferred material. However, it was found that the process of depositing CsI:Tl could damage the CMOS surface. Gd_2O_2S:Tb was therefore chosen as it has desirable characteristics and can be bonded to the CMOS sensors.

Property	Example scintillator	
	CsI-Tl 55 μm thick – Al reflector	Gd_2O_2S:Tb 25 mg/cm^2 – Al reflector
Relative efficiency	0.68	0.96
MTF @ 8 lp/mm (%)	65.8	54.5
MTF @ 12 lp/mm (%)	42.0	28.1
Absorption edge	medium – 33 kV	high – 50 kV
Density (g/cm^3)	4.5	7.6
Structure/ particle size	columnar poly-crystal	direct deposit particle, 4 μm med

Table 18: Sample comparative specifications of two scintillator configurations investigated for use. [55]

Optimizing the scintillator performance will have a large effect on the final image quality and resolution achievable from HEX-ID. The effectiveness of the scintillator will be tested in the Excalibur facility using the existing 15-pin d-type vacuum feed-through connections on the chamber to connect a CMOS sensor, test box, cRIO system and laptop running the LabView program. The sensor can be exposed to the x-ray source and can measure reflections off the crystals.

4.0 CONCLUSIONS & FURTHER WORK

A innovative soft x-ray spectrometer for short and long-pulse laser plasma interactions, HEX-ID, has been designed with high confidence to provide high resolving power imaging, with remote deployment and operation, within a vacuum and short-pulse laser environment, while also being compatible for use within TIMs on the Orion laser facility at AWE (UK) and on the OMEGA laser at LLE (USA). The HEX-ID diagnostic will be used to: observe x-ray emission lines to determine the thermodynamic state of the emitting plasma; measure the opacity of the plasma; verify x-ray backlighter materials; perform absolute conversion efficiency measurements of laser energy to x-rays from a solid target; and identify plasma ion species and their charged states by using the relative heights and widths of spectral features.

The key aspects of the design taken into consideration and decided upon include details of the crystals selected, filter materials, collimation, energy dispersion, x-ray spectral range and maximising the resolving power performance.

The extraction of the desirable soft x-rays to be diagnosed from the laser-produced plasma will be carried out using: magnets in the nosecone to deflect and remove unwanted high energy particles; Tungsten collimation at various locations throughout the diagnostic to direct the x-rays towards the crystals and then detectors, a Beryllium debris shield to protect the crystals and other components with the diagnostic; metal filter materials to select particular energy ranges for each of the four channels; and Perspex covering the internal walls to minimise fluorescence.

Convex reflection crystal geometry was used, as with the Henway and HENEX x-ray spectrometers, to allow a compact design and provide the necessary high resolving power. Four convex reflection crystals are used to disperse the x-rays onto the detector plane. Exact values for some of the parameters resulted from the size of the spectrometer nosecone, the positioning of the crystals within the instrument and the fielding of the instrument at Orion. Other parameters, such as the crystal to detector

distance (*f*) and the radius of curvature of the crystals (*r*), were adjusted in models to find the optimal values. X-ray emission from a laser-plasma experiment, in the range of 1.2 to 9.8 keV, will be obtained when the *f* value is set to its maximum (166.2 mm), which achieves a theoretical resolving power of $E/\delta E \approx 1200$. Using the minimum *f* value (139.2 mm) will allow a similar spectral range to be obtained for two types of detector fielded simultaneously, each occupying half of the active area with the resolving power is reduced to approximately 730. The front half will capture 1.2 to 8.3 keV with a small gap between 2 and 2.2 keV, while the rear half will capture 2 to 9.8 keV.

Users will be able to select various combinations of image plate, CMOS and PCD detectors to obtain the desired information from laser-plasma experiments. The different detectors that will be used in HEX-ID are: Fuji BAS TR image plate (IP); Rad-icon Imaging Corporation Radeye 1 CMOS sensors; and Alameda Applied Sciences Corporation Diamond Radiation Detectors (PCD). Pre-constructed modules will allow quick insertion into the spectrometer before deployment of the diagnostic. This means the dynamic range of the spectrometer can be adapted for long-pulse and short-pulse laser shots; cross-channel comparison of the energy dispersion and spectral range can be performed; and the desired spectral and temporal resolution can be acquired.

IP will provide time-integrated data where the energy dispersion and spectral range are more important considerations than resolution achievable, such as during commissioning tests. It can also be used to make relative comparisons of line emissions on the same piece of image plate for a given laser shot. IP also provides a large dynamic range and it is immune to damage or interference that can be induced by an electromagnetic pulse environment. Although the dynamic range of the CMOS sensors is smaller than for image plate, the sensor has higher quantum efficiency and due to it being electronic, there is no additional processing time to record the data following a laser shot. The PCDs are to be moveable to align with particular characteristic energies and this will allow the temporal evolution of the x-ray flux in the energy range within each channel to be recorded.

Fielding the electronic sensors (CMOS and PCD) requires hardware, cabling and software. A processing unit will be contained within an airbox behind the spectrometer in the TIM to meet the CMOS sensor requirements. This was a CompactRIO system from National Instruments with suitable modules. The PCDs require a high voltage (~300 V) bias to be supplied to the SMA cables connecting the detectors to an oscilloscope capable of at least 5 GHz. Electromagnetic interference (EMI)/ electromagnetic pulse (EMP) protection is required for the electronic components utilised in the design of HEX-ID. Shielding will be implemented by covering the entire instrument (including the nosecone) in an Aluminium skin, which will act as the Faraday cage to block external electric fields.

The signal intensities expected from a laser shot at the Orion and Omega facilities were calculated allowing for the selection of appropriate thicknesses of filter materials for each channel. The method for aligning the diagnostic with the target prior to a shot involves using a compact laser pointer with the diagnostic. Confirmation of the laser pointer details still needs to be carried out. The Orion target chamber port that would be used for fielding HEX-ID was decided upon, the vacuum compatibility of the finished design was analysed, and the overall mass of the diagnostic and whether it would meet the TIM specifications required consideration. Final filter thicknesses need to be identified following the final characterisation work of individual components.

Characterisation of key components was carried out towards the end of the project. This involved determining the best type of image plate for use in the finished spectrometer, measuring the x-ray reflectivity of the convex reflection crystals and determining the resolution of the CMOS sensors.

Five different types of image plate from two manufacturers were sourced for a resolution comparison study and the Manson x-ray facility at AWE was used to carry out these experiments. Exposed image plates were scanned by the Fuji FLA3000 and FLA7000 scanners allowing spatial resolution comparisons between different image plate systems. On comparison between the various types of image plate investigated,

it is clear that the Fuji BAS TR IP has the highest resolution at 4.95 keV. This was followed in order by the Fuji SR, Fuji MS, Kodak XL and Kodak HR. The use of the Fuji FLA7000 scanner has improved the maximum achievable resolution for all types of IP compared to the FLA3000. As the TR IP was found to have the highest contrast transfer function and best resolution, it will be used with the HEX-ID spectrometer when it is in operation and scanned using the Fuji FLA7000 scanner.

The peak locations and integrated reflectivity of x-rays from the convex crystals attached to their mounts was measured at several energies in the range 0.5 to 8 keV using the Excalibur soft x-ray facility at AWE. The peak positions for the x-rays reflected off the Quartz, Silicon and Germanium crystals were recorded in their expected positions. Peak positions for the Beryl crystal could not be determined due to the appearance of two peaks in the recorded data at the same location despite changing the x-ray energy. It is thought that the two peaks relate to fluorescence from Silicon and Aluminium present within the Beryl crystal. Time constraints prevented further investigation of the Beryl crystal. The integrated reflectivity values were calculated to range between 0.158% and 0.014%, with the order of decreasing crystal reflectivity being Germanium then Silicon then Quartz. This was the expected order based on information provided by the manufacturer. There would appear to be a general trend of increasing reflectivity when higher energy x-rays are incident on the crystal surface. No value was obtained for the Beryl crystal due to the lack of x-ray reflections.

The CMOS sensor was also tested to determine its resolution limit in the visible spectrum. Upon comparison with the IP resolution tests it was seen that for visible light the CMOS sensor can achieve the same resolution of 35.0 μm as the Fuji BAS TR image plate exposed to x-rays. There is also a significant improvement in the contrast transfer function at this resolution. From this work it would appear that the Radeye 1 CMOS sensors can meet the requirements of providing resolving power and allowing remote imaging. Appropriate scintillator materials need to be ordered for the CMOS sensors and tested in the Excalibur soft x-ray facility to determine the resolution achievable in the x-ray spectrum.

The two large areas of work still to be done before HEX-ID is operational are the assembly and commissioning tests. The assembly stage will involve the following sub-areas: check over the completed CAD design before sending drawings to manufacturers; receive two spectrometer bodies after manufacture; collect all necessary components to fit out the bodies; check the crystal fixings, detector platform and aperture have been machined as intended; check fitting of all components and alignment of pinhole with laser pointer; assemble detector modules and check they fit in the detector platform; confirm EMP shielding is adequate; fit the crystals to the spectrometer and practice removing and inserting filters; check the detectors can be connected to the cable bulkhead as required; and finally fit all the components within the airbox, make the necessary wiring connections and evaluate airbox leak rate to verify vacuum suitability. The commissioning tests stage requires locating a facility that can be used to test the whole spectrometer. This may be possible using the Excalibur facility at AWE, one channel at a time without the nosecone attached. Absolute calibration experiments will need to be carried out to measure the spectral range and sensitivity, while verifying the achievable resolving power, after which HEX-ID will be ready for use on Orion.

5.0 REFERENCES

[1] L. N. Koppel and J. Deleckels, Bulletin of the American Physical Society **22**, 1112 (1977)

[2] J. Seely, C. Back, R. Deslattes, et al., Review of Scientific Instruments **72**, 2562 (2001)

[3] J. Wark, *The AWE Introductory Course in Plasma Physics* (Department of Physics, University of Oxford, 2004), p. 141

[4] D. Giulietti and L. A. Gizzi, Rivista Del Nuovo Cimento **21**, 1 (1998)

[5] A. R. Bell, *Plasma Physics: An Introductory Course*, edited by R. Denby, p. 319

[6] *Laser-plasma interactions*, edited by D. A. Jarosynski, R. Bingham and R. A. Cairns (CRC Press, Vol. SUSSP60, p. 1)

[7] Short-pulse matter interaction, AWE Intranet, visited September 2011

[8] N. Hopps, T. Bett, N. Cann, et al., PPD Annual Report 2010 (2010)

[9] Orion Facility, AWE, visited September 2011, http://www.awe.co.uk/set/Laser_facilities.html

[10] G. Brumfiel, Nature **464**, 156

[11] T. J. Goldsack, *The ORION laser at AWE: progress, likely experiments, and diagnostics* (68th Scottish Universities Summer School in Physics – Laser-Plasma Interactions and Applications, University of Strathclyde, Glasgow, 2011)

[12] OMEGA Laser Facility, Laboratory for Laser Energetics, visited September 2011, http://www.lle.rochester.edu/omega_facility/

[13] O. L. Landen, D. R. Farley, S. G. Glendinning, et al., Review of Scientific Instruments **72**, 627 (2001)

[14] P. Pavan, G. Zanella, R. Zannoni, et al., Nuclear Instruments & Methods in Physics Research Section a-Accelerators Spectrometers Detectors and Associated Equipment **327**, 600 (1993)

[15] Private Communication with J. Seely, NIF, Capabilities & status of the HENEX, Diagnostic x-ray spectrometer for NIF

[16] Private Communication with A. L. Meadowcroft, AWE

[17] Private Communication with A. Simons, S. Mcalpin, E. Kerswill, et al., AWE

[18] J. F. Seely, C. I. Szabo, U. Feldman, et al., Review of Scientific Instruments **81**, 3 (2010)

[19] C. I. Szabo, L. T. Hudson, A. Henins, et al., Radiation Physics and Chemistry **75**, 1824 (2006)

[20] E. J. Gamboa, D. S. Montgomery, I. M. Hall, et al., Journal of Instrumentation **6**, 14

[21] F. N. Chukhovskii, K. T. Gabrielyan, E. N. Kislovskii, et al., Physica Status Solidi a-Applied Research **103**, 381 (1987)

[22] J. F. Seely, L. T. Hudson, G. E. Holland, et al., Applied Optics **47**, 2767 (2008)

[23] *Laser-Induced Breakdown Spectroscopy*, edited by J. P. Singh and S. N. Thakur (Elsevier, p. 94)

[24] Radeye1 Large Area Image Sensor, Rad-icon Imaging Corp, visited September 2011, www.rad-icon.com/pdf/RadEye1.pdf

[25] Diamond Radiation Detector Catalog, Alameda Applied Sciences Corporation, visited September 2011, http://www.aasc.net/media/DRD-Catalog.pdf

[26] S. G. Gales and C. D. Bentley, Review of Scientific Instruments **75**, 4001 (2004)

[27] A. L. Meadowcroft, C. D. Bentley, and E. N. Stott, Review of Scientific Instruments **79**, 4 (2008)

[28] Document AN05: High-resolution CMOS imaging detector, Rad-icon Imaging Corp, visited September 2011, www.rad-icon/pdf/Radicon_AN05.pdf

[29] Diamond Radiation Detectors, Alameda Applied Sciences Corporation, visited September 2011, http://www.aasc.net/media/DRD-AppNote.pdf

[30] R. B. Spielman, L. E. Ruggles, R. E. Pepping, et al., Review of Scientific Instruments **68**, 782 (1997)

[31] A. S. Cross, J. P. Knauer, A. Mycielski, et al., Nuclear Instruments & Methods in Physics Research Section a-Accelerators Spectrometers Detectors and Associated Equipment **624**, 649 (2010)

[32] Private Communication with P. Thomas, AWE

[33] What is CompactRIO? – Understanding the CompactRIO Architecture, National Instruments, visited September 2011, http://www.ni.com/compactrio/whatis/

[34] M. J. Mead, D. Neely, J. Gauoin, et al., Review of Scientific Instruments **75**, 4225 (2004)

[35] D. C. Eder, R. W. Anderson, D. S. Bailey, et al., *Sixth International Conference on Inertial Fusion Sciences and Applications, Parts 1-4* (Iop Publishing Ltd, Bristol), Vol. 244

[36] C. G. Brown, A. Throop, D. Eder, et al., *5th International Conference on Inertial Fusion Sciences and Applications*, edited by H. Azechi, B. Hammel and J. C. Gauthier (Iop Publishing Ltd, Bristol, 2008), Vol. 112

[37] A. N. Tait, *Data Analysis for Electro-Magnetic Pulse (EMP) Measurements* (Laboratory for Laser Energetics, University of Rochester, New York, 2007)

[38] C. G. Brown, E. Bond, T. Clancy, et al., *Sixth International Conference on Inertial Fusion Sciences and Applications, Parts 1-4* (Iop Publishing Ltd, Bristol, 2010), Vol. 244

[39] P. G. Burkhalter, F. C. Young, B. H. Ripin, et al., Physical Review A **15**, 1191 (1977)

[40] D. Duston, R. W. Clark, and J. Davis, Physical Review A **31**, 3220 (1985)

[41] D. W. Phillion and C. J. Hailey, Physical Review A **34**, 4886 (1986)

[42] U. Andiel, K. Eidmann, K. Witte, et al., Applied Physics Letters **80**, 198 (2002)

[43] Z. Zhang, H. Nishimura, T. Namimoto, et al., Review of Scientific Instruments **83**, 5

[44] A. P. Fews, P. A. Norreys, F. N. Beg, et al., Physical Review Letters **73**, 1801 (1994)

[45] B. Westover, A. MacPhee, C. Chen, et al., Physics of Plasmas **17**, 5

[46] Document AN10: QE Measurements of the RadEye1 Image Sensor, Rad-icon Imaging Corp, visited August 2011, www.rad-icon.com/pdf/Radicon_AN10.pdf

[47] S. Han, R. S. Wagner, and E. Gullikson, Nuclear Instruments & Methods in Physics Research Section a-Accelerators Spectrometers Detectors and Associated Equipment **380**, 205 (1996)

[48] M. Thoms, H. Vonseggern, and A. Winnacker, Physical Review B **44**, 9240 (1991)

[49] Private Communication with Austin Instruments inc., Manson Model 5 Multianode Ultrasoft X-ray Source Installation and Operating Instructions

[50] Private Communication with S. G. Gales and C. D. Bentley, AWE

[51] Private Communication with A. W. J. Thompson, AWE

[52] Private Communication with C. D. Bentley, AWE

[53] X-ray Interactions with Matter - X-ray Transmission of a Solid, The Center for X-ray Optics, visited September 2011, http://henke.lbl.gov/optical_constants/filter2.html

[54] Document AN07: Scintillator Options for Shad-o-Box Cameras, Rad-icon Imaging Corp, visited September 2011, www.rad-icon.com/pdf/Radicon_AN7.pdf

[55] Application note – x-ray imaging 1 (Optimising x-ray imaging performance using columnar CsI:Tl vs phosphor depositions, Applied Scintillation Technologies Ltd, visited September 2011, http://www.appscintech.com/sites/default/files/applicationnoteX-rayimaging1%28Dental%29-iss1.pdf

APPENDIX

A.1 HEX-ID Project Plan Document

1. Literature search on past HENWAY and HENEX diagnostics, as well as short-pulse laser-target interactions
2. Review of user requirements and basis of design
    i. Crystals
    ii. Detection system
    iii. Crystal and detector integration
    iv. Shielding requirements and spectrometer geometry
3. Basic design review
4. Detailed design
    i. Crystals and shielding
    ii. Detection and electronics
    iii. TIM integration
5. Further physics model development
6. Testing and calibration
7. Assembly and commissioning
8. First experiment with the HENWAY

A.2 MAPLE Calculation of Resolving Power

R="E*(-r*cos(-arcsin(1/2*hc/d/E)+arcsin((s-1/2*r*(4-hc^2/d^2/E^2)^(1/2))/H))*(hc/d/E^2/(4-hc^2/d^2/E^2)^(1/2)-1/2*r*hc^2/(4-hc^2/d^2/E^2)^(1/2)/d^2/E^3/H/(1-(s-1/2*r*(4-hc^2/d^2/E^2)^(1/2))^2/H^2)^(1/2))+r*sin(-arcsin(1/2*hc/d/E)+arcsin((s-1/2*r*(4-hc^2/d^2/E^2)^(1/2))/H))*(hc/d/E^2/(4-hc^2/d^2/E^2)^(1/2)-1/2*r*hc^2/(4-hc^2/d^2/E^2)^(1/2)/d^2/E^3/H/(1-(s-1/2*r*(4-hc^2/d^2/E^2)^(1/2))^2/H^2)^(1/2))/tan(-2*arcsin(1/2*hc/d/E)+arcsin((s-1/2*r*(4-hc^2/d^2/E^2)^(1/2))/H))+(r*cos(-arcsin(1/2*hc/d/E)+arcsin((s-1/2*r*(4-hc^2/d^2/E^2)^(1/2))/H))-f)*(1+tan(-2*arcsin(1/2*hc/d/E)+arcsin((s-1/2*r*(4-hc^2/d^2/E^2)^(1/2))/H))^2)*(2*hc/d/E^2/(4-hc^2/d^2/E^2)^(1/2)-1/2*r*hc^2/(4-hc^2/d^2/E^2)^(1/2)/d^2/E^3/H/(1-(s-1/2*r*(4-hc^2/d^2/E^2)^(1/2))^2/H^2)^(1/2))/tan(-2*arcsin(1/2*hc/d/E)+arcsin((s-1/2*r*(4-hc^2/d^2/E^2)^(1/2))/H))^2)/`Δg`"

A.3 Wiring Diagram for CMOS Test Box

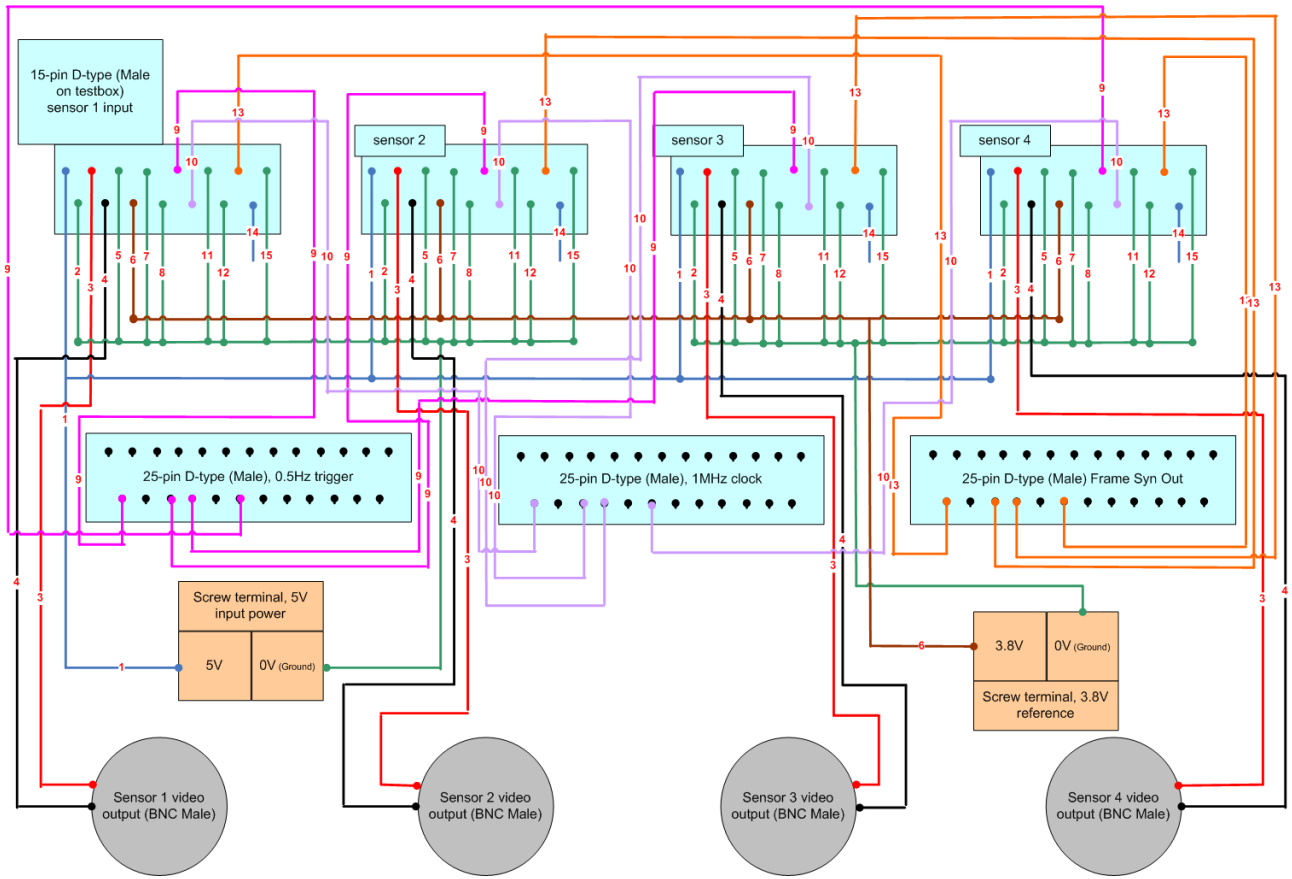

Figure 49: CMOS test box wiring diagram detailing connections in the test box in order for the cRIO to control four sensors. [16]

A.4 Resolution of USAF Test Target

Element	Group Number									
	-2	-1	0	1	2	3	4	5	6	7
1	0.250	0.500	1.00	2.00	4.00	8.00	16.00	32.0	64.0	128.0
2	0.280	0.561	1.12	2.24	4.49	8.98	17.95	36.0	71.8	144.0
3	0.315	0.630	1.26	2.52	5.04	10.10	20.16	40.3	80.6	161.0
4	0.353	0.707	1.41	2.83	5.66	11.30	22.62	45.3	90.5	181.0
5	0.397	0.793	1.59	3.17	6.35	12.70	25.39	50.8	102.0	203.0
6	0.445	0.891	1.78	3.56	7.13	14.30	28.50	57.0	114.0	228.0

Table 19: Number of line pairs/mm for each group and element on a 1951 USAF resolution test target.

Element	Group Number									
	-2	-1	0	1	2	3	4	5	6	7
1	2000	1000	500	250	125	62.5	31.3	15.6	7.8	3.9
2	1785.7	891.3	446.4	223.2	111.4	55.7	27.9	13.9	7.0	3.5
3	1587.3	793.7	396.8	198.4	99.2	49.5	24.8	12.4	6.2	3.1
4	1416.4	707.2	354.6	176.7	88.3	44.2	22.1	11.0	5.5	2.8
5	1259.4	630.5	314.5	157.7	78.7	39.4	19.7	9.8	4.9	2.5
6	1123.6	561.2	280.9	140.4	70.1	35.0	17.5	8.8	4.4	2.2

Table 20: Pixel size (μm) for each group and element on a 1951 USAF resolution test target.